Mechanical Modeling of Gradient Materials

Gyula Béda[1, a] and Peter B. Béda[2,b]

[1]Department of Applied Mechanics, Budapest University of Technology and Economics, Hungary

[2]Department of Vehicle Elements and Vehicle-Structure Analysis, Budapest University of Technology and Economics, Hungary

[a]beda@mm.bme.hu, [b]bedap@kme.bme.hu (corresponding author)

Keywords: Constitutive equations, thermodynamics, continuum mechanics, dynamics

Abstract. Gradient materials get more and more importance in both material science and numerical studies of technological processes. Their mathematical model is called the constitutive equation. The theoretical background of such model is presented on the basis of thermodynamics and continuum mechanics. The results show which is the quantity to measure to get constitutive equation for gradient dependent materials.

Introduction

The constitutive equations of mechanics connect the data of material testing to each other. In a uni-axial stress state these are stress σ, strain ε, strain rate $\dot{\varepsilon}$, stress rate $\dot{\sigma}$. Such quantities appear at tensile test, when stress-strain diagram is drawn and during creep and relaxation. The new results of material science lead to the use of new materials with definite internal structure effects. As examples

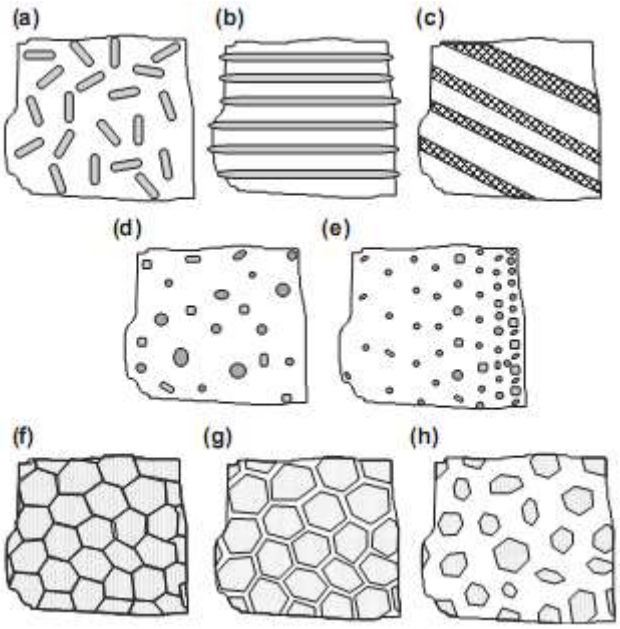

Fig.1 A few types of gradient materials [3]

from the literature Fig. 1. shows various types of composites: a) short-fiber, b) long fiber, c) layered, d) particle, e) functionally gradient material, f) polycrystalline with different fracture properties of grain boundary, g) polycrystalline with small interfaces, and h) polycrystalline with thick interfaces.

On the other hand computational methods require constitutive equations with derivatives to x,y,z. In Fig.2 the results of the numerical analysis of a material instability problem [4] is presented. Here the necking zone has a finite length. With no gradient effects this length shows mesh dependence. It means that the length of the instability zone is determined by the mesh size, which

has no physical meaning. This effect is avoided by “gradient regularization”, which can be considered as a formal inclusion of gradient terms

$$\varepsilon_x = \frac{\partial \varepsilon}{\partial x} \text{ or } \varepsilon_{xx} = \frac{\partial^2 \varepsilon}{\partial x^2}.$$

Materials with constitutive equations consisting of such terms are called gradient materials.

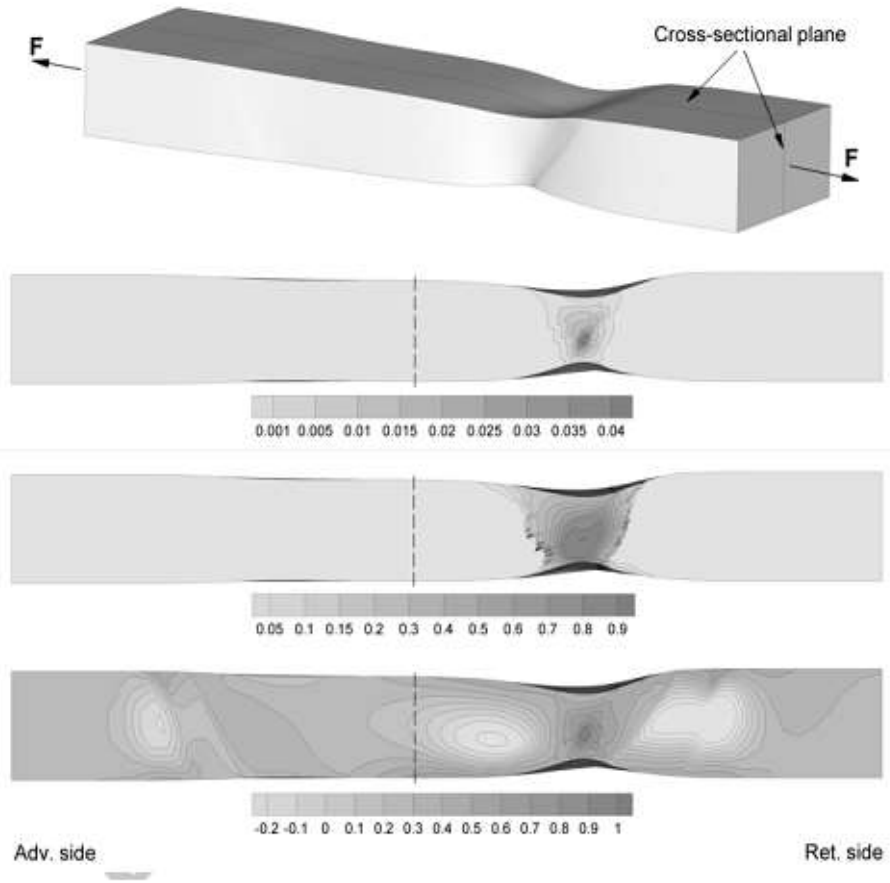

Fig.2 Numerical results for necking instability [4]

First and second gradient dependence

The most popular gradient constitutive equation

$$\left(\cdot \quad \frac{\partial^2 \cdot}{\partial x^2} \cdot \quad \frac{\partial}{\partial t} \right)$$

has a second gradient dependent term, For numerical studies its discretized form is an anticipatory system [5]

$$\sigma_{i+1} = C\varepsilon_{i+1}, \quad \text{where} \quad \left(C = D + \tilde{C} \frac{\partial^2}{\partial x^2} \right) \tag{1}$$

To perform a numerical analysis two more equations should be added. These are the discretized versions of the Cauchy equation of motion and of the kinematic equation,

$$v_{i+1} = v_i + \frac{1}{\rho}\frac{\partial \sigma}{\partial x}\bigg|_i \Delta t \tag{2}$$

where volumetric forces are neglected and

$$\varepsilon_{i+1} = \varepsilon_i + \frac{\partial v}{\partial x}\bigg|_i \Delta t\,. \tag{3}$$

From Eq. 1, Eq. 2 and Eq. 3 a discrete dynamical system should be defined

$$\begin{bmatrix} v_{i+1} \\ \varepsilon_{i+1} \\ \sigma_{i+1} \end{bmatrix} = A \begin{bmatrix} v_i \\ \varepsilon_i \\ \sigma_i \end{bmatrix}, \quad \text{where} \quad A = \begin{bmatrix} 1 & 0 & \frac{1}{\rho}\Delta t \frac{\partial}{\partial x} \\ \Delta t \frac{\partial}{\partial x} & 1 & 0 \\ C\Delta t \frac{\partial}{\partial x} & C & 0 \end{bmatrix}.$$

Eigenvalues λ_k of operator A determine the stability properties. When the constitutive equation is Eq. 1 the stability investigation results a non-generic way of loss of stability. It is presented in Fig.3, where the arrows show how the

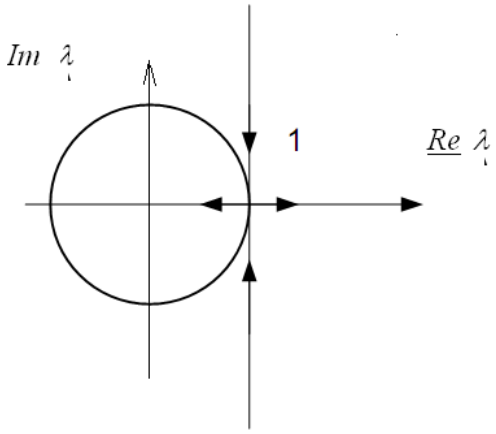

Fig.3 Non-generic way of instability

locations of eigenvalues changes, when tangent stiffness D is varied. One of them remains always mostly outside the unit disc, that is, there is no stability except the case $\lambda = 1$.

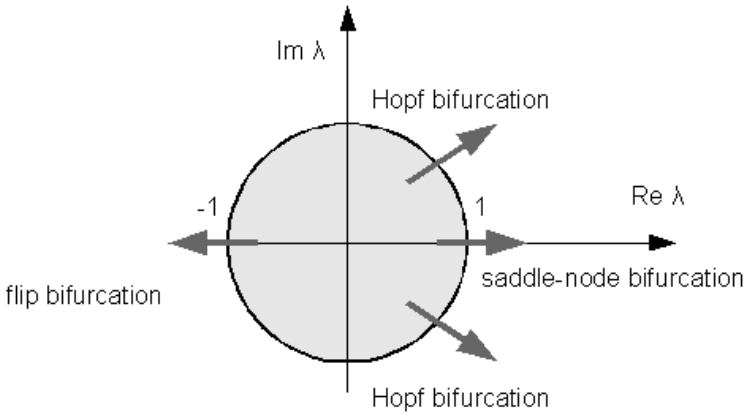

Fig.4 Generic instability modes

In contrary Fig. 4 shows the generic case with various types of bifurcations for discrete dynamical systems. Here the stable case is reached, when all the eigenvalues are inside the unit disc (grey). Loss of stability happens, when at least one of them leaves it. Instability happens as one of the generic bifurcations depending on the location of the exit. If Figs. 3 and 4 are compared, we see that Eq. 1 result a non-generic behavior. No real stable cases and no regular bifurcations can be detected. Such constitutive equation case serious difficulties and mistakes in numerical analysis.

To summarize we find that some theoretic basis is needed to determine and measure a quantity to show ε_x dependence. In the following such possibility will be presented using the laws of thermodynamics, because mechanical deformations are always coupled with thermodynamic processes.

Variational principles and virtual work

In his pioneering work Mindlin [1] derived a constitutive equation for gradient materials from variational principles. He used the principle of virtual work and the principle of complementary virtual work

$$\int_t \int_V \sigma : \delta\varepsilon dV dt \quad \text{and} \quad \int_t \int_V \varepsilon : \delta\sigma dV dt \tag{4}$$

expressions $\sigma : \delta\varepsilon$ and $\varepsilon : \delta\sigma$ for an elastic body can be calculated in uniaxial case from

$u(\varepsilon)$ elastic potential and from

$u^*(\sigma)$ complementary elastic potential as

$$\sigma\delta\varepsilon = \frac{\partial u}{\partial \varepsilon}\delta\varepsilon \quad \text{or} \quad \varepsilon\delta\sigma = \frac{\partial u^*}{\partial \sigma}\delta\sigma$$

that is,

$$\sigma = \frac{\partial u}{\partial \varepsilon} \text{ and } \varepsilon = \frac{\partial u^*}{\partial \sigma} .$$

Assume that elastic potential is completed with the first law of thermodynamics in form

$$w_1 = 0,$$

then

$$\sigma\delta\varepsilon = L_\varepsilon\left(u + \lambda w_1\right)\delta\varepsilon,$$

and for stress

$$\sigma = L_\varepsilon\left(u + \lambda w_1\right) \tag{5}$$

where L_ε denotes the Lagrange operator

$$L_\varepsilon(\,) = \left(\frac{\partial}{\partial \varepsilon} - \frac{d}{dt}\frac{\partial}{\partial \dot{}} - \frac{d}{\quad}\frac{\partial}{\quad}\right)(\,).$$

The second term of Eq. 5 is expressed from the first law of thermodynamics

$$w_1(\varepsilon,\vartheta)=\rho \cdot \quad \cdot \quad \cdot .$$

Here notations are:

ϑ - temperature,
ρ - mass density,
e internal energy,
h heat flux,
r heat source intensity,
s entropy product,
$h_x=\dfrac{\partial h}{\partial x}$.

Now similarly as before (in case of Eq. 5) ε can be expressed, but here complementary energy and work is used (the second formula of Eq. 4)

$$\varepsilon=L_\sigma\left(u+\lambda w_1^*\right).$$

In this expression the form of the first law of thermodynamics uses Gibbs function G and entropy S ,

$$w_1^*(\sigma,\vartheta)=\rho(G-\vartheta S)^{\square}-(\quad \quad)$$

for the derivatives

$$(\quad \quad \varepsilon)^{\square} \text{ and } \vartheta \quad \cdot \quad ,$$

where a denotes Green's elastic potential.

Having done the necessary calculations stress and strain can be obtained,

$$\sigma=\rho\left(\frac{\partial a}{\partial \varepsilon}+\vartheta\frac{\partial S}{\partial \varepsilon}\right)+\frac{1}{\cdot}\left(\rho\vartheta\frac{\partial S}{\cdot} \quad \right)\frac{r}{\cdot} \tag{6}$$

and

$$\varepsilon=-\frac{1}{\cdot}\left(\rho(G \quad \quad \quad \quad -\sigma_x+h_\vartheta\vartheta_x-\rho r\right). \tag{7}$$

By multiplying the equation Eq. 7 by

$$E=\frac{\cdot}{\cdot}$$

and adding to Eq. 6

$$\sigma+E\varepsilon=\rho\left(a_\varepsilon+\vartheta S_\varepsilon-EG_\sigma\right)+\rho\left(\vartheta S_\vartheta-G_\vartheta\right)\frac{\cdot}{\cdot}+\frac{1}{\cdot}\left(h_\varepsilon-h_\sigma\sigma_x\right) \tag{8}$$

is obtained.

Discussion

In expression Eq. 8 $\dot{}$ must be different from zero. In standard tensile test speed v_0 at which the specimen is pulled is a prescribed small value. When the length of it is ℓ, strain rate is nonzero, but small, thus strain rate is usually given as

$$\dot{} \quad \frac{v}{\ell} \quad . \tag{9}$$

Remark that is such case $\frac{\partial \dot{}}{\partial x} = \upsilon$, thus approximation Eq. 9 cannot be used in gradient materials.

For small strain rate term

$$\frac{h_\varepsilon \varepsilon_x}{\dot{}}$$

is large, thus we have a gradient material and if heat flux can be measured as function of strain, h_ε can be calculated and the constitutive equation of the gradient material is obtained.

In material testing mechanical motion and thermodynamic processes are coupled, but in most cases thermodynamic effects may be neglected, when compared to mechanical phenomena.

Summary

For modeling gradient materials rate dependent terms are necessary in the constitutive equation. When thermodynamics is taken into consideration a general form of such equation was derived. For practical applications the data of this equation can be obtained by measuring heat flux as function of strain. If such measurement can be performed, a physically and mathematically correct mathematical model is found for gradient materials, which is available for further numerical studies.

Acknowledgements

The work of the second author was supported by the National Scientific Research Funds of Hungary (OTKA contract number: K81531)

References

[1] R.D. Mindlin, Second gradient of strain and surface tension in linear elasticity, Intl. Journal of Solids and Structures, 1 (1965) 417-438.

[2] Gy. Béda, Thermomechanical stress from conditional Lagrange derivative, Per. Polytechnica, Mech. Eng. 56/1 (2012) 7-8.

[3] T.Sadowski, L. Marsavina, Multiscale modelling of two-phase Ceramic Matrix Composites, Computational Materials Science 50 (2011) 1336-1346.

[4] K.L. Nielsen, T. Pardoen, V. Tvergaard, B. de Meester, A. Simar, Modelling of plastic flow localisation and damage development in friction stir welded 6005A aluminium alloy using physics based strain hardening law, International Journal of Solids and Structures, 47 (2010), 2359–2370.

[5] R Rosen, Anticipatory Systems. Pergamon Press. New York, 1985.

Estimation of Thermal Boundary Conditions by using Hybrid Inverse Approach

Imre Felde[1, a]

[1]John von Neumann Faculty of Informatics, Óbuda University, Budapest, Hungary

[a]felde.imre@nik.uni-obuda.hu

Keywords:IHCP, heat transfer coefficient, optimization, hybrid approach

Abstract. The estimation of thermal boundary conditions occurring during heat treatment processes is an essential requirement for characterization of heat transfer phenomena. In this work, the performance of five optimization techniques is studied. These models are the Conjugate Gradient Method, the Levenberg-Marquardt Method, the Simplex method, the NSGA II algorithm and a hybrid approach based on the NSGA II and Levenberg-Marquardt Method sequence. The models are used to estimate the heat transfer coefficient in 2D axis symmetrical case during transient heat transfer. The performance of the optimization methods is demonstrated using numerical experiments.

Introduction

Immersion quenching operation is widely applied in the industry to change materials properties under high temperatures and high rates of cooling, a condition in which the heat transfer can be dominated by the cooling characteristics of the cooling media. To attain the required heat transfer conditions, exactly known thermal loads must be supplied on the material surface, namely design surface, and thus both the temperature and the heat flux are prescribed. The problem consists of determining the specifications for the heat exchange to achieve the desired conditions on the design surface. Performing inverse heat conduction problem (IHCP) analysis [1-4] the required information for the heat transfer process can be achieved.

The IHCP of immersion quenching has been usually tackled by either implicit or explicit formulation. In the implicit approach, the problem is formulated as a multivariable optimization problem, while the explicit formulation attempts to determine directly the unknown parameters with the use of regularization techniques to solve the resulting system of equations. There are two distinct groups of optimization techniques: the deterministic methods (Conjugate Gradient [3], Levenberg-Marquardt [4], Simplex [5], etc) and the stochastic approaches (genetic algorithms [6], particle swarm optimization [7,8] etc.).

In general, deterministic methods are faster than stochastic methods, although they are more prone to converge to a local instead of the global minima or maxima. On the other hand, stochastic algorithms, despite being more likely to converge to the global minima or maxima, are in general expensive computationally. Various optimization techniques have been applied to estimate the heat transfer during quenching process as well. This study is focusing on a hybrid solution that combines two approaches: the stochastic method, by which the global minimum in the search space can be localized and the deterministic formulation, which is for the swift find the global optimum.

The heat conduction model

The mathematical formulation of the transient heat transfer for a homogeneous isotropic domain (Ω) is defined as follows:

$$\nabla \cdot \left(k(\mathbf{r},T)\cdot \nabla T\right)+Q(T,\mathbf{r},t)=C_p(\mathbf{r},T)\rho(\mathbf{r},t)\frac{\partial T}{\partial t} \tag{1}$$

where $\mathbf{r}\in\Omega$ is the spatial vector, t is the time, k is the thermal conductivity, T is the temperature, C_p is the specific heat, ρ is the density and Q is the latent heat. The initial condition is

$$T(\mathbf{r},t=0)=T_0(\mathbf{r}) \tag{2}$$

where T_0 is the initial temperature of the domain. The boundary conditions are expressed by:

$$-k\frac{\partial T}{\partial \mathbf{r}}=h_i\left(T(\mathbf{r},t)-T_{am}\right) \quad \text{in}\,\Gamma_i i=1\ldots p \tag{3}$$

where h_i are the heat transfer coefficients corresponding to different portions of the boundary ($\Gamma_1\cup\Gamma_2\ldots\cup\Gamma_p=\Gamma$ and $\Gamma_1\cap\Gamma_2\ldots\cap\Gamma_p=\varnothing$) and T_{am} is the ambient temperature.

Inverse heat conduction scheme

Assuming that the temperature inside the work piece and/or on its surface is measured during the heat transfer process, it is possible to solve the inverse heat conduction problem by determining the time / or temperature variations of the thermal boundary conditions[1-3].Each one of domain boundary zones Γ, is considered to have a time dependent heat transfer coefficient, $h_i(t)$. The time dependence of the heat transfer coefficient can be approximated by polynomial functions, each one defined by a set of parameters $h_i^{(r)}$ = (r=1…p; i=1…q), according to Fig. 1. The unknown design parameters can be expressed by the vector of *m* (*m*= *p*q*), components $\boldsymbol{\tau}$ = $(\tau_1,\ldots,\tau_m)$ = $(h_1^{(1)}, \ldots, h_q^{(1)}, h_1^{(2)}, \ldots, h_q^{(2)}, \ldots, h_1^{(p)}, \ldots, h_q^{(p)})$. The temperature at different times is given by measurements at *n* points in the solid region, located at $\mathbf{r}_k$,(k=1…n). On calling T_k^m, the measured temperatures, and T_k^c, the calculated temperature at those points, one can pose the problem of obtaining the values of the heat transfer coefficients $\tau_i$that minimize the cost function, S:

$$S=S(\tau_1,\ldots,\tau_m)=\sum_{k=1}^{n}\left(T_k^m-T_k^c\right)^2=\min \tag{4}$$

where*n* is the total number of measured temperatures, i.e., the number of points multiplied the number of measurements at each point.

Hybrid approach

The solution of the Inverse Parameter Estimation Problems is based on the minimization of equation (4). The following optimization approaches have applied used to minimize the value of S:

1. Simplex (**Simplex**) search method is based on the Nelder–Mead algorithm [5]
2. Levenberg-Marquardt Method (**LMM**) [4]
3. Conjugate Gradient Method (**CGM**) [3,4,9],
4. The Non-dominated Sorting Genetic Algorithm (**NSGA II**) [10-12]
5. Hybrid method using (**NSGA II**) and (**LMM**) is sequentially

According to Fig.1., the iterative computational procedure for the estimation of HTC can be summarized as follows:

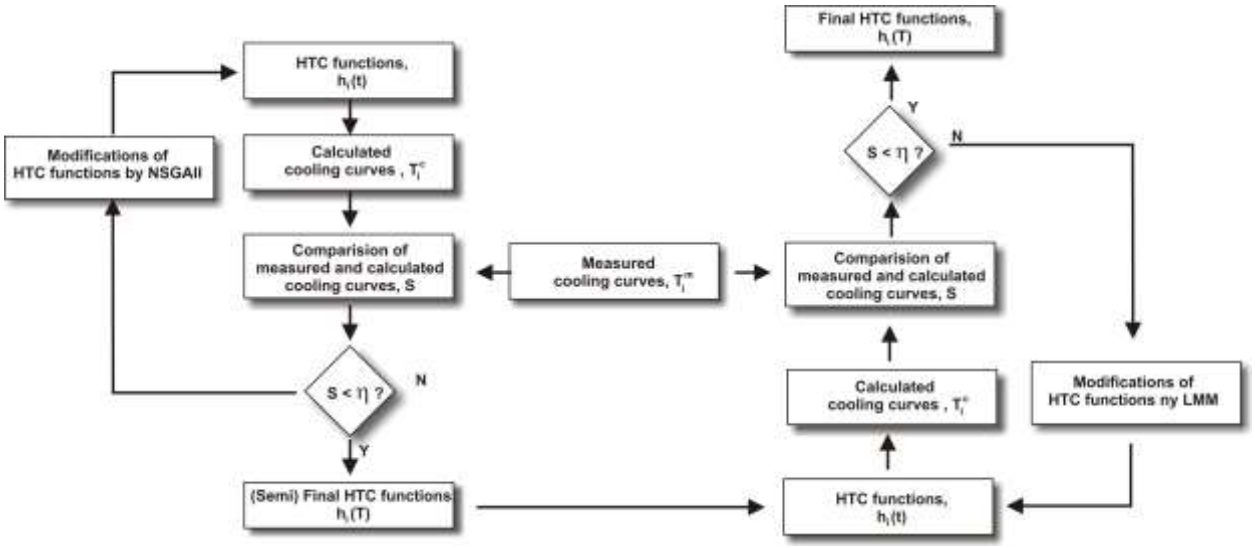

Figure 1 The iterative procedure for the determination of thermal boundary conditions

The following steps are obtained by using the optimization methods if they used by their own (Simplex, LMM, CGM and NSGAII):

Step 1 During the initial iteration, the components of the vector τare initialized to some values
Step 2 The values of $h_i(t)$ functions are set
Step 3 The cooling curves (T_k^c) are calculated based on numerical simulation
Step 4 The difference between the measured (T_k^m) and the calculated (T_k^c) time-temperature signals are characterized by calculating S
Step 5 If the value of S is greater than a desired tolerance value (η) then the $h_i(t)$ functions are modified by using the optimization algorithm and a new iteration is started at Step 2. If S is less than η then the iteration stops.

The Hybrid approach is also based on the Steps 1-5 while the output results of Step 5 will be the input data for the temperature field computations. The Hybrid method requires the following additional steps:

Step 6 The cooling curves (T_k^c) are calculated based on numerical simulation
Step 7 The difference between the measured (T_k^m) and the calculated (T_k^c) time-temperature signals are characterized by calculating S
Step 8 If the value of S is greater than a desired tolerance value (η) then the $h_i(t)$ functions are modified by using the LMM algorithm and a new iteration is started at Step 6.
If it is so than the final estimated $h_i(t)$ functions are estimated

Numerical example and discussion

In order to compare the performance of the optimization algorithms on the prediction of thermal boundary conditions, two numerical experiments for the quenching process have been performed. In the analysis, there was no physical set-up to directly measure the temperature T_k^m. Instead, we assume theoretical heat transfer coefficient functions, $h_i(T)$ and substitute them directly into the equations (1)–(3) to calculate the temperatures at each location for the thermocouples (TC). The

results are used in the computed temperature T_k^m curves. Due to this concept the T_k^m curves have been assumed to be error-free samples. The following concepts have been used for the computational investigations:

- The theoretical $h_i(T)$ functions have been determined
- The T_k^m temperature signals have been generated by obtaining simulations on the basis of $h_i(T)$ functions
- Inverse computations have been carried out by applying each optimization method, in order to reconstruct the original $h_i(T)$ functions
- The computational results were analysed

The quenching process for a cylindrical work piece, mounted with 5 TC's was investigated. A 2D axis-symmetric heat transfer model was applied to calculate the temperature distribution during the cooling process. The physical properties of Inconel 600 alloy were assigned to the workpiece. The thermocouples were assumed to be mounted at 1 mm below the side surface of the rod. The location of the TC's (the distances from the bottom of the cylinder) and the parameters used for the calculations are summarized in Table 1. The effect of wetting front kinematics that occurs during immersion quenching, is taken into consideration, by defining the heat transfer coefficient [14,15] $h_i(T,z)$, which is assumed to be dependent on temperature and the vertical local coordinate, Eq.(5).

$$h_i(T,z)=\begin{cases} 5500*\exp\left\{-\exp[-11.34*(T-400)^2+500]\right\} & T\le 400°C \\ 5500*\exp\left\{-\exp[(-11.34+0.0606*z-2.653*10^{-4}*z^2)*(T-400)^2+500]\right\} & T>400°C \end{cases} \quad (5)$$

The theoretical $h_i(T,z)$ as predefined, is represented at Fig. 2., while the cooling curves obtained at the TC locations are shown at Fig. 3. The $h_i(T,z)$ is used for all the surfaces of the work piece including the top and the bottom faces as well. For the inverse calculations 100 components of the vector $\boldsymbol{\tau}$ have been applied, while the initial estimate of $h_i(T,z)$ was set to 100 $Wm^{-2}K^{-1}$. The population size was defined to 100, for the NSGA II method.

Radius, R	25 mm	TC 1	z = 0 mm
Length, L	200 mm	TC 2	z = 50 mm
Initial temperature, T_0	850 C°	TC 3	z = 100 mm
Ambient temperature, T_{am}	50 C°	TC 4	z = 150 mm
Locations of TC 1-5 below the surface	r=R-1	TC 5	z = 200 mm

Table 1. Parameters applied for the computational example

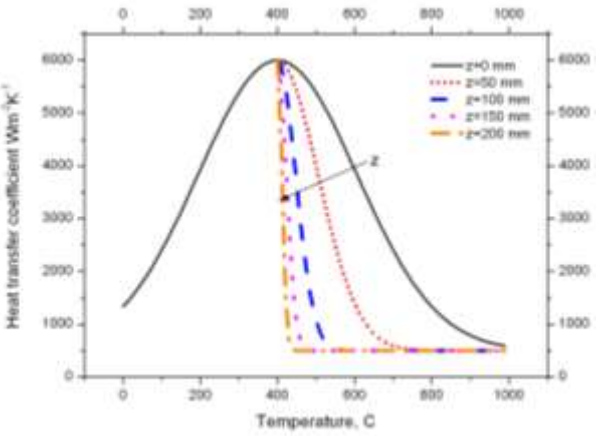

Figure 2. The theoretical heat transfer coefficient function applied

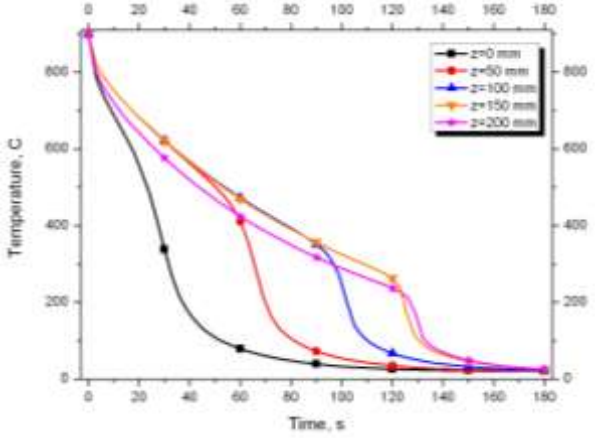

Figure 3. The predicted cooling curves obtained at the TC locations in direction of axis "z"

In order to reconstruct the thermal boundary conditions 500 generations were investigated by the NSGA II model and 400 iterations were performed by the LMM, CGM and Simplex models (Fig. 4.). The concept of using the Hybrid approach was to perform the generations until the cost function exceeds $2.0*10^4$, or $1.5*10^4$, $1.0*10^4$ and then the iteration was continued by means of LMM. Then the LMM calculations were carried out till the S was lower than 100 or the number of LMM iterations exceed 150.

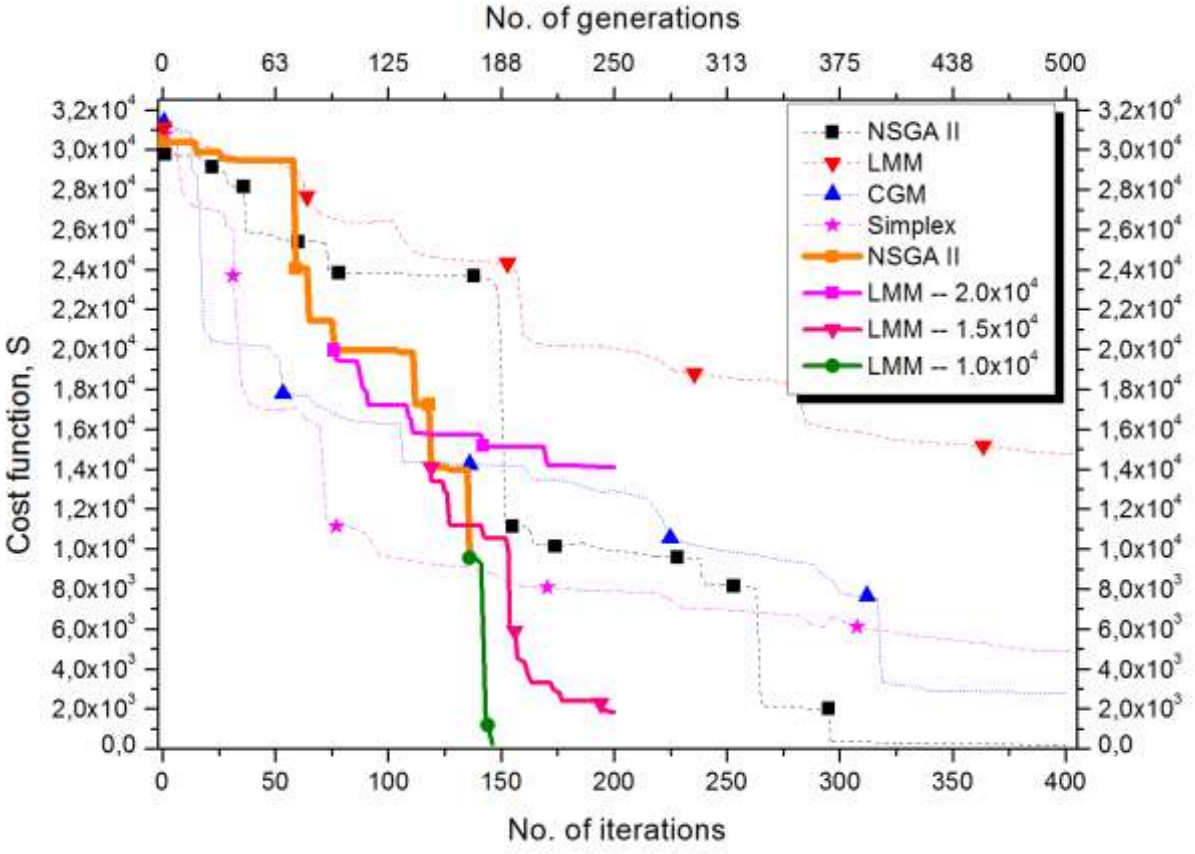

Figure 4. The evolution of cost function (S), as functions of iterations and generations

The results obtained by Simplex, LMM and CGM showed a limited accuracy for the inverse estimation. The discrepancy of the predicted heat transfer coefficient were still unacceptable huge after the 400 iterations. Very good agreement between the original and recovered HTC functions was given by using the NSGAII algorithm. However, at least 300 generations had to be built to achieve the desired output. The fastest convergence with the highest recovery performance was given by using the hybrid optimization sequence when the NSGAII method was used until the value of S was lower than $1.0*10^4$. Similar results but slower convergence obtained in the case of LMM -- $1.5*10^4$, while rather big S belongs to LMM -- $2.0*10^4$.

The reason for the poor agreement between the measured (pre-calculated) and estimated temperature curves is due to the complexity of the heat transfer phenomena, where the boundary conditions of the third type varied with the surface temperature, as well as, the distance measured from the bottom of the work piece. These results point out that the inverse heat transfer calculations applied for sophisticated thermal problems needs robust numerical methods to achieve a desirable outcome.

Summary

In this work, the performance of five different optimization models for the estimation of heat transfer coefficients during an immersion quenching process have been compared. An automatic optimization procedure based on a process simulator, cost function and various numerical

optimization techniques was used. The optimizations methods applied were the Simplex, Conjugate Gradient Method, Levenberg-Marquardt Method, NSGAII method and a hybrid approach based on a NSGAII-LMM sequence. The performance of the optimization algorithms is compared using on a numerical test, where the thermal boundary condition of the third type was functions of surface temperatures and local coordinates. The best prediction was given by the hybrid method as well as the NSGAII algorithm, however the later one required more computational efforts. It must be noted that the results performed by using LMM, CGM and Simplex techniques are strongly depend on the initial set of parameters [6,7]. The more smaller the difference between the initial guess functions and the HTC functions to be estimated the more faster convergence of the cost function and more accurate prediction of boundary conditions can be performed. However, our investigation is based on the concept that no any preliminary knowledge has been given about the HTC functions. These assumptions comprise the parameter intervals and isolation of the search space. With finer isolations, the applied methods would most likely perform differently. Testing the methods on different isolations remains a task for further investigation.

Acknowledgement
We acknowledge the financial support of this work by the Hungarian State and the European Union under the TÁMOP-4.2.1. B -11/2/KMR-2011-0001 and TÁMOP-4.2.2/A-11/1-KONV-2012-0029 projects.

References

[1] J.V. Beck, B. Blackwell, C.R. St Clair Jr., Inverse Heat Conduction, Wiley, New York, 1985.
[2] A.N. Tikhonov, V.Y. Arsenin, Solution of Ill-posed Problems, Winston, Washington, DC, 1977.
[3] O.M. Alifanov, Inverse Heat Transfer Problems, Springer, Berlin/Heidelberg, 1994.
[4] M.N. Özisik, H.R.B. Orlande, Inverse Heat Transfer: Fundamentals and Applications, Taylor & Francis, New York, 2000.
[5] J.A. Nelder, R. Mead, A simplex method for function minimization, Comput. J. 7 (1965) 308–313.
[6] J.C. Lagarias, J.A. Reeds, M.H. Wright, P.E. Wright, Convergence properties of the Nelder–Mead simplex method in low dimensions, SIAM J. Optimiz. 9 (1996) 112–147.
[7] R. Das: A simplex search method for a conductive–convective fin with variable conductivity, International Journal of Heat and Mass Transfer 54 (2011) 5001–5009
[8] O. Nelles, Nonlinear system identification, Springer-Verlag, Berlin, 2001.
[9] Fletcher, R. and Reeves C. M., "Function Minimization by Conjugate Gradients," Computer J. 7 (1964) 149-154
[10] K. Deb, A. Pratap, S. Agarwal, T. Meyarivan, A fast and elitist multiobjective genetic algorithm: NSGA-II, IEEE Transactions on Evolutionary Computation 6 (2002) 182–197.
[11] K. Deb, Multi-objective Optimization Using Evolutionary Algorithms, Wiley Chichester UK 2001.
[12] D.A.V. Veldhuizen, G.B. Lamont, Multi-objective evolutionary algorithms: analyzing the state-of-the-art, Evolutionary Computation 8 (2000) 125–147
[13] J. Clark and R. Tye: “Thermophysical properties reference data for some key engineering alloys”. High temperatures – high pressures 35/362003/2004 1-14.
[14] A. Majorek, B. Scholtes, H. Müller, E. Macherauch: Influence of heat transfer on development of residual stresses in quenched steel cylinders Steel research 41994 146-151
[15] H. M. Tensi, A. Stick : Martens hardening of steel - Prediction of temperature distribution and surface hardness, Materials Science Forum 102-104 (1992) 741-75

Practical Aspects of Micromechanics Based Simulation of Polymer Matrix Composites

Zoltan Major[1], Martin Reiter[1] and Michael Jerabek[2]

[1]Institute of Polymer Product Engineering, Johannes Kepler University
Altenberger Str. 69, 4040 Linz, Austria

[2]Borealis Polyolefine GmbH, Linz, Austria

zoltan.major@jku.at (corresponding author)

Keywords: micromechanics, mean field homogenization, representative volume element, particle filled and fiber reinforced polymer matrix composites

Abstract. As particle filled and fiber reinforced polymer matrix composites are frequently used in many demanding industrial applications, the proper prediction of the deformation behavior of these materials is of high practical importance for a reliable product design. To predict the thermo-mechanical behavior, micromechanics based simulations were performed using both the mean field homogenization methods (MFH) and full-scale finite element (FS-FE simulations on a material specific representative volume. The applicability and limitations of both methods are introduced based on five different practical examples. Both thermoplastic polymers and elastomers were used as matrix materials with combination of fillers made from different materials having different aspect ratio and revealing a wide variation of alignments and arrangements. While conventionally the behavior of composites revealing processing induced microstructure is predicted for practical engineering applications, novel artificial micro-structures revealing special functionalities might also be designed and their behavior predicted for supporting material development efforts.

Introduction

Particle filled and fiber reinforced polymer matrix composites play an essential role in many demanding engineering applications and provide an essential contribution towards sustainable and environment friendly product development. In addition to the experimental characterization, numerical simulations may support both product design and material development efforts. The various fillers generates a highly heterogeneous and in many cases also highly anisotropic microstructure. The optimization of this anisotropy is a key factor for improving the complex time and temperature dependent thermo-mechanical behavior of these materials.

Furthermore, the experimental characterization of these materials along with results for various polymer matrices, fillers, and interface compatibilization methods are described and discussed in details in many publications [1-3]. The mechanical behavior of these materials was typically characterized in tensile tests using standardized specimen configurations. The main dependencies and functions are well-known for a number of technically relevant polymer compounds and composites. These specimens reveal, however, only a narrow range of microstructure configurations and these are not always relevant for practical components. The wide variety of possible microstructures in components cannot be exclusively characterized by conventional experimental methods. Moreover, computational homogenization methods were developed over the last decades and are increasingly used for practical purposes. The theoretical, material science and computational aspects of these methods are summarized in numerous publications and books [4-6]. The objective of this paper is to shortly review several practical aspects of the micromechanics based material modeling of particle filled and fiber reinforced polymer composites by the means of selected examples.

Finally, it must be emphasized that in principle all simulations, but specifically the micromechanics simulations have to be verified by appropriate experiments. Several examples related to this paradigm of the authors provided also in this paper.

Models

Particulate fillers revealing various shapes/aspect ratio values and discontinuous as well as continuous fibers over a wide length scale are frequently used for stiffening polymer matrix materials. These compounds and composite materials are widely used in many demanding engineering applications (e.g. automotive, mechatronics, medical, oilfield). The real microstructure which was generated during the processing (i.e. injection molding or lamination) can be characterized by non-destructive image generating methods (e.g. scanning electron microscopy 2D and computed tomography 3D). Due to the significant development of these methods over the last decade, the microstructure details of heterogeneous materials can easily and successfully be characterized for engineering purposes up to a length scale of several hundred nanometers [7, 8]. Scanning electron microscopy images of Polypropylene composites filled with particles (glass beds, talc platelets and wollastonite fibers) revealing different aspect ratio values are shown in figure 1.

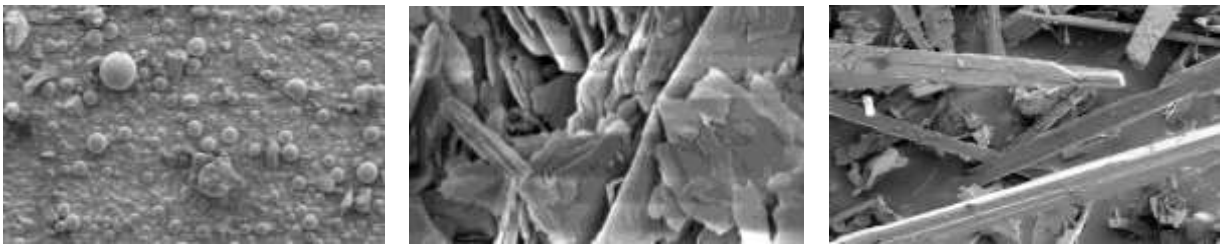

Fig. 1: Scanning electron microscopy images of particles revealing different shape and aspect ratio (AR) values. All types of particles all widely used in polymer matrix composites.

Due to the injection molding conditions a typical layer-like structure (skin-core-skin) is observed for discontinuous short/long fiber reinforced injection molded composites [9-11]. While stiffening of the compounds is always observed if the fillers reveal higher modulus than the embedding matrix material, lower stiffness is observed for softer filler materials (i.e. elastomer particles). Furthermore, with increasing volume fraction there is an increase of the stiffness [1, 2, 12, 13]. The shape/aspect ratio of the particles also significantly influences the stiffness, and the anisotropy of the compound. With increasing aspect ratio an increase of the stiffness was observed in the relevant direction (fiber orientation). Simultaneously the transversal and shear modulus became significantly lower. Based on the images of the actual microstructure a direct or an indirect reverse engineering process can be designed and performed.

- *Direct method*
  The distribution of the particles and all components of the fiber orientation tensor (FOD) can be determined after a real processing using image analysis. This specific microstructure can be modeled either in a mean field homogenization based or in a full-scale finite element based simulation tool. In both cases, however, simplifications are used. The agreement between the simulation and the results essentially depends on the fact how close the model is to the real microstructure, the quality of the material model and the model parameters and the coincidence of the loading and boundary conditions in the experiment and simulations.
- *Indirect method*
  In a CAD file an unlimited variety of spatial distribution and orientation of fillers/fibers can be realized. This artificial microstructure can be implemented into the micromechanics models. An optimum target function property or function combination (i.e. optimal stiffness

and toughness or optimal stiffness with optimal heat conductivity) is scrabbled. This method can also be successfully applied in a sensitivity analysis manner, that is, the processing parameter-structure-property relationship might be analyzed. The remaining question is for "nice-to-have" structures for targeted specific applications the realization of these microstructures in real processes.

The orientation and the location of the particles can be determined by applying a 1D fixed fiber orientation, a 2D or 3D fiber orientation tensor, a 2D or 3D random fiber distribution function. Schematic representation of the definition of fiber orientations and alignments is shown in figure 2. In addition to the real process induced microstructure configurations tailor made microstructures can also be designed. Various principles for this design may be applied:

- Spherical particles (AR=1) can be placed in regular chains and the distance of these particle chains may also be varied
- If platelet-like particles are used, this stacking process may generate column like structures in one direction and staggered structures in the other.
- Fiber like particles can also be positioned in a staggered structure. Staggering is a building principle of the nature (nacre, bone) and staggered platelet containing systems are optimized for stiffness and toughness in the nature.

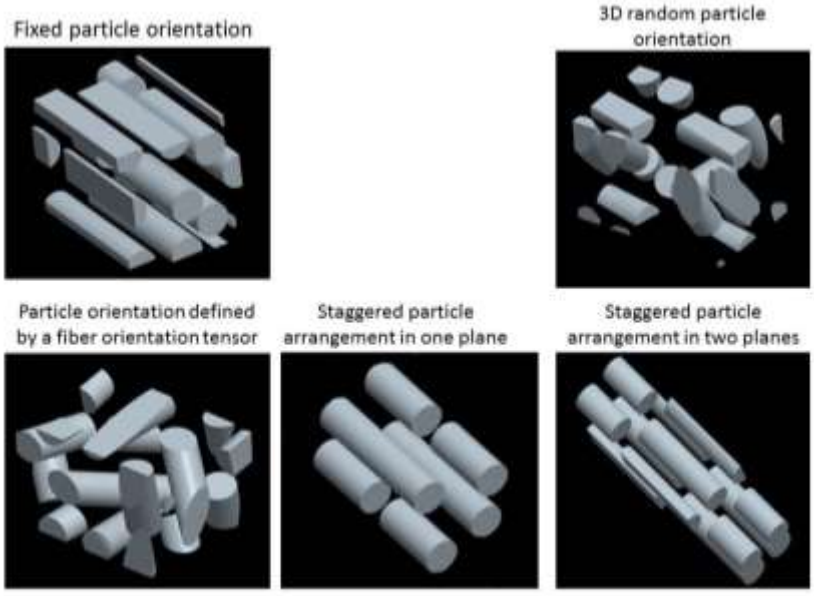

Fig. 2: Schematic representation of various fiber alignments and arrangements in microcells.

Methodology and Objective

The schematic representation of the overall methodology is shown in figure 3. The objective of the micromechanics based simulation is the generation of a representative volume which reflects the global macroscopic behavior of the selected heterogeneous material. However, there are significant differences from both theoretical, simulation technique and practical point of view between the mean field homogenization (MFH) method and the full-scale finite element (FS-FE) method. While the MFH provides only the global deformation response of the selected representative element, the FS-FE microcell is able to determine both the local stress/strain distribution around the inclusions and the global response of the selected volume element. The efficient application of FS-FE is time consuming and requires a high performance computing.

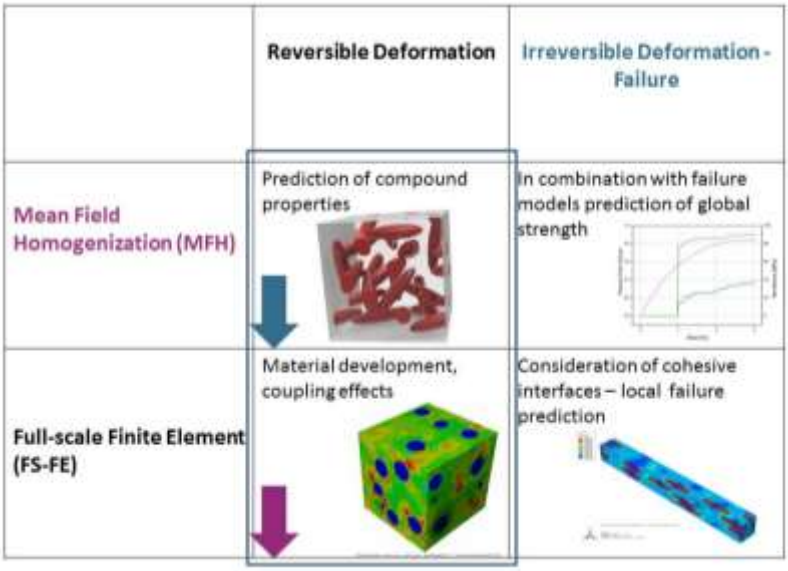

Fig. 3: Schematic representation of the micromechanics based simulation methodology.

Based on our experiences, the reversible deformation response in the linear elastic regime can easily and accurately be predicted using both methods by applying proper material models for the polymer matrix and filler particles used. Significantly complicated is, however, the prediction of the irreversible deformation or failure behavior. To gain more insight into these topics we can suggest the following literatures [14-16]. The increasing complexity and several specific aspects of MFH and FS-FE simulations are introduced by 5 examples in the paper.

Examples

Simulation Example 1: Mean Field Homogenization with various particle shapes in the linear viscoelastic deformation range for polypropylene compounds, direct method

A mean field homogenization (MFH) module of the software tool DigiMat-MF (eXstream enginnering, Foetz, LX) was applied for determining the linear elastic deformation behavior of various particle filled PP(H) composites over a wide test temperature (-30 up to 80 °C) and over a wide loading rate range (10^{-4} up to 1 mm/s) in the first example. The comparison of the tensile tests and the MFH simulations is shown in figure 4 in terms of tensile modulus values.

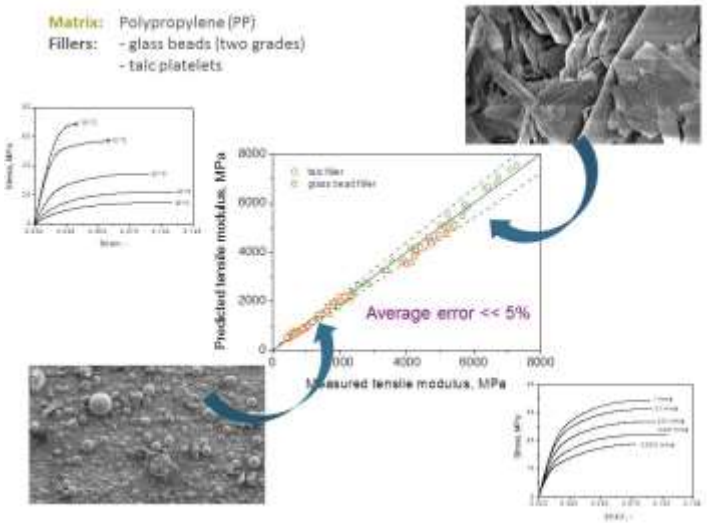

Fig. 4: Comparison of experimental results and mean field (MF) homogenization based simulations of glass bead (spherical particles with AR=1) and talc particles (platelets with AR=0.05) filled Polypropylene (PP) compounds. The tensile test were performed for all materials over a wide test temperature (-30 up to 80 °C) and over a wide loading rate range (10^{-4} up to 1 mm/s).

As it is clearly shown in this figure, based on carefully conducted experiments and appropriate simulations, the difference between predictions and experiments is less than 5 % over a very wide tensile modulus range (loading rate and temperature combination) for both compounds. For more details please refers to [14, 15]. In addition to other stiff thermoplastic matrix (i.e. PTFE, PA, PEEK) based compounds and composites, particle filled elastomeric materials were also modeled. As examples, two different methods are described and shortly discussed in the next section of this paper.

Simulation Example 2: FS-FE; simulations of magnetoelastomers with distributed (isotropic) and with aligned (anisotropic) particles; direct method

Magnetoelastomers were developed based on various elastomeric matrix materials and magnetic filler particles by various research groups [16-20]. To predict the influence of the filler on the stiffness of the elastomers both with and without magnetic field various micromechanics based simulations were performed by the research group of the authors. While several results of the simulations without magnetic field are reported previously [21-23] and here also shortly, the method and the first simulations within magnetic field using a fully coupled magneto-elasto-static approach in a finite strain framework is reported recently in [24]. Furthermore, it was reported in many papers if the filler particles are evenly distributed in the matrix, the macroscopic response of the magnetoelastomer is isotropic. In addition, the magnetic particles may be aligned in the magnetic field during the curing process. This results in a chain-like particle arrangement which generates a highly anisotropic mechanical behaviour. Moreover, it was found that external magnetic field influences the mechanical behaviour significantly higher for anisotropic magnetoelastomers than for isotropic ones [25]. The experimental comparison of storage modulus values for isotropic and for anisotropic particles with and without magnetic field is shown in the diagram in figure 5. The microcells represent these situations. These microcells were generated in the finite element module of the same software tool (DigiMat FE) and the cells were implemented into the finite element tool Abaqus 6.12 (Simulia).

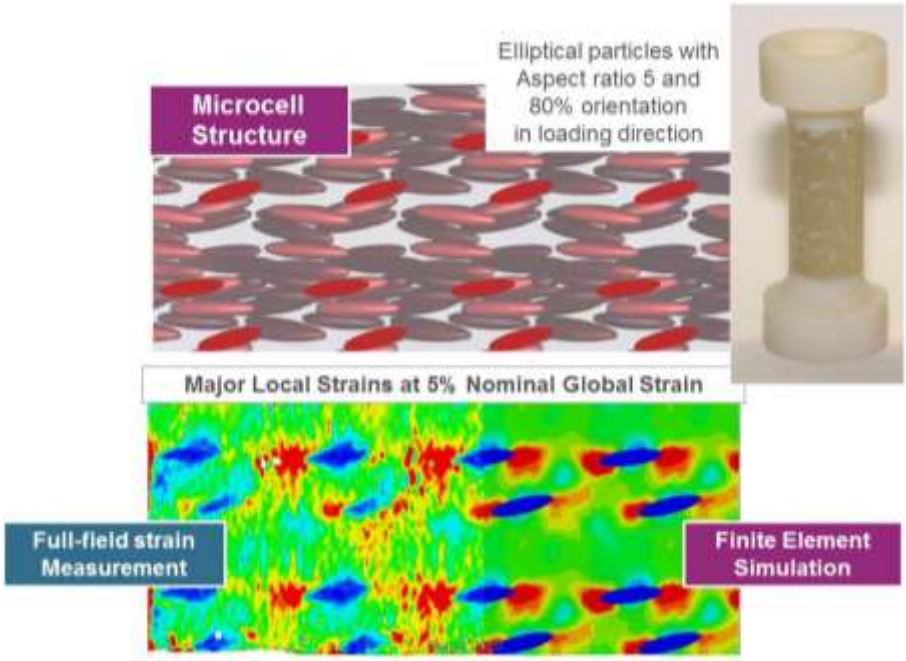

Fig. 5: Comparison of storage modulus of values for isotropic and anisotropic particle filled magnetoelastomers. Representation of the corresponding microcells with spherical and platelet-like particles.

Simulation Example 3: FS-FE modeling; Prototyping of microcells with various particle orientations; indirect method

A novel material structure prototyping method was developed and implemented by the authors and described in details in [26]. To contribute to the verification efforts of the micromechanics based simulations, a novel 2-component 3D prototyping technique may be applied for printing these microcells using a proper combination of hard and soft matrices and particles. A wide variety of material microstructures was realized by using this technique. The microcells were shaped into convenient test specimens and subsequently tested under various loading conditions. Furthermore, micromechanics simulations on various microcell configurations were performed and the virtual deformation behavior was characterized. The CAD design of an artificial microcell is shown in the upper part of figure 6. This microcell was realized as test specimen (right upper corner) and was tested. The same configuration was simulated in the FE tool. The comparison of the simulation and the experimental results in terms of local strain at the surface of the microcell is shown in the lower part of the figure.

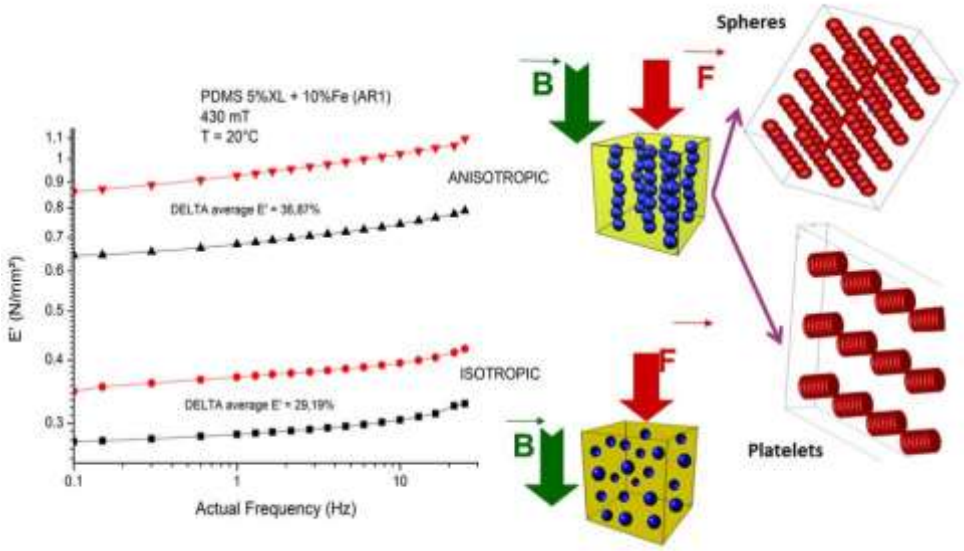

Fig. 6: Prototyping of a heterogeneous microstructure. Experimental measurement and finite element simulation of local strain distributions at the microcell surface.

Simulation Example 4: FS-FE modeling; Staggered particles in an elastic matrix; indirect method

Staggered particle arrangements are recognized in many biological objects. The mineral platelets in nacre or the mineralized collagen structures of a bone follow the periodicity of the staggering and are combined with thin layers of soft tissues. This combination results in an optimized stiffness and toughness for these structures. Several theoretical and experimental investigations are reported in the relevant literature along with theoretical considerations for toughening mechanisms [27, 28]. Based on above publications, microcells containing fiber like particles with low AR values in staggered arrangements were generated by using FS-FE models. In contrary to the biological objects, the matrix material behavior was assigned as PP and the particles as glass and a significantly lower particle volume fraction was defined (25 % in spite of 70-80 %). The staggered arrangement was realized both in one and in two planes using both rectangular and cylindrical particles. The deformation behavior of the staggered microcells was predicted and compared typical conventional particle arrangements. As expected the microcell with fixed perfect orientation revealed the highest stiffness in fiber orientation direction. The multiplication of the staggered planes increased the stiffness significantly. All microcells were investigated in fiber orientation direction, in transvers direction and in shear mode (1-2 and 2-3). Further results are described and discussed elsewhere [29].

Simulation Example 5: FS-FE modeling; application of a complex 3D particle shape in an elastomer matrix, application of a combined hyper- viscoelastic material model; indirect method.

Typically, particles with natural shapes (mineral particles) or fibers are used as fillers in many practical applications. In addition, particles revealing special functional shapes might also be designed and used. Without realizable manufacturing techniques, however, the application of these particles is limited in computer simulations. One exceptional example is provided.

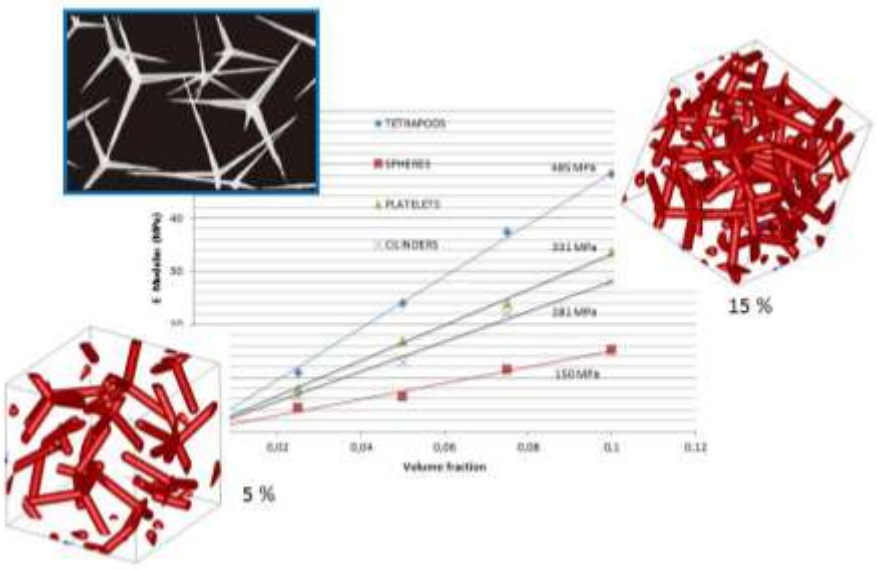

Fig. 7: Filler volume fraction dependence of the elastic modulus for various filler aspect ratios and geometries. The SEM image and the microcells of the tetra-pod filler with 5 and 15 V% filler content.

By ZnO_2 single crystals (whiskers) which reveal a special shape termed as tetra-pod and these particles are produced on an industry scale [30] and incorporated into thermoplastic and elastomer matrices for several technical applications. The tetrapod shape might generate special behavior termed as balanced anisotropy. The filler volume fraction dependence of the elastic modulus is shown for various filler aspect ratios and geometries in figure 7. As it was expected and in good agreement with many experimental results [1] with increasing volume fraction a linear increase of the modulus was observed. The tetra-pod fillers are also shown in the corresponding images (microscopy and microcells with 5 and 15 V%) and the tetra-pod compounds revealed the highest stiffness. As it was mentioned previously, the simulations in the reversible deformation regime can not only be performed by applying linear-elastic material models. The Three-Network model proposed by Bergström and implemented in PolyUMod 1.9.0 [31] was used to predict the combined hyper-viscoelastic deformation behavior of the elastomer matrix pana-tetra compounds. In our actual research work, pana-tetra fillers with surface compatibilization for polypropylene and for NBR and HNBR grade elastomers will be compounded and these compounds will be experimentally investigated in form of convenient test specimens under various loading conditions. These results will be used for verifying above results in the near future.

Summary

Mean field homogenization theory and full-scale finite element simulations are frequently used in novel micromechanics simulation for supporting material development efforts for designing novel polymer matric composites for demanding industrial applications.

Representative volume elements (termed also as microcells) can either be constructed based on real material microstructures or designed artificially using various target functions. In the direct engineering method the process relevant microstructures are implemented in to the microcells and the deformation behavior of these heterogeneous compounds and composites are predicted and compared to relevant experiment. Based on comprehensive research work the accuracy of these predictions is in general above 95 % over a wide temperature, loading rate range and for a wide variety of matrix and filler materials in the linear elastic reversible deformation regime.

The reverse engineering concept might also be applied for micromechanics simulation. Artificial microcells for various target functions (i.e. optimized stiffness and toughness, optimized stiffness and heat conductivity, optimized magnetic effect, optimized tribological behavior heat conductivity, friction and strength) can be designed and simulated. To fulfill these requirements in addition to proper material properties, spatial particle arrangements, specific particle shapes are needed. The objective of further research is to find such optimized microcells configurations which can be realized under real processing conditions.

Acknowledgement

The research work described in this paper was performed in various research projects (K_{APMT} and ACCM) of the authors and supported by company partners (Borealis Polyolefine GmbH, Linz, A; Eckart, Velden, D and E. Mach Gummitechnik, Hirm, A). Special appreciation goes to Franz Hiptmair, Anna Kalteis, Matthias Eckerstorfer and Juan Pablo Torres for preparing specimens and performing experiments and simulations.

References

[1] Móczó, J., Pukánszky, B.: Polymer micro and nanocomposites: Structure, interactions, properties. J. Ind. Eng. Chem., 14, 535-563 (2008).

[2] K. Renner, J. Moczó and B Pukanszky, Micromechanical Deformation Processes in Polymer Composites: Measurements andpractical Consequences, APST1, July 2009, Linz, in Proceedings of a Conference on Polymer Science (eds. Schwarzinger and Brüggemann)

[3] A.M. Hartl et al. “Comparison of methods to characterize damage onset in short glass fiber filled polypropylene”, ICCM19, Montreal, Canada, 2013.

[4] Eshelby J. D.: The determination of the elastic field of an ellipsoidal inclusion, and related problems. Proc. Roy. Soc. A, 241, 376-396 (1957).

[5] Doghri, I. et al. “Mean-field based on a general incrementally affine linearization method”. International Journal of Plasticity, Vol. 26, pp 219-238, 2010.

[6] Wing Kam Liu Cahal McVeigh, Predictive multiscale theory for design of heterogeneous materials, Comput Mech (2008) 42:147–170, DOI 10.1007/s00466-007-0176-8.

[7] D. Salaberger, K. Kannappan, J. Kastner, J. Reussner and T. Auinger, “CT Data evaluation of fibre reinforced polymers to determine fibre length distribution”. Intern. Polymer Processing, Vol. 3, 283-291, 2011.

[8] M. Schossig et al. “ESEM investigation for assessment of damage kinetics of short glass fiber reinforced thermoplastics - Results of in situ tensile tests coupled with acoustic emission analysis”, Composites Science and Technology, Vol 71, pp 257-265, 2011.

[9] Martuscelli E.: Structure and properties of polypropylene-elastomer blends. In ‘Polypropylene structure, blends and composites 2’ (ed. Karger-Kocsis J.) Chapman & Hall, London, 95-140 (1995).

[10] S.-Y. Fu, B. Lauke, Y.-W. Mai “Science and engineering of short fiber reinforced polymer composites”. Woodhead Publishing, Cambridge, UK, 206-219, 2009.

[11] J.-K. Kim, Y.-W. Mai “Engineered interfaces in fiber reinforced composites”. Elsevier, Oxford, UK, 239-277, 1998.

[12] M. Jerabek et al. “Characterization of short fiber reinforced polypropylene composites”. 15th European Conference on Composite Material, Venice, Italy, 2012
[13] M. Jerabek, Z. Major, K. Renner, J. Móczó, B. Pukánszky and R. W. Lang, Filler/matrix-debonding and micro-mechanisms of deformation in particulate filled polypropylene composites under tension, Polymer 51 (2010) 2040-2048.
[14] S. Kammoun et al. “First pseudo-grain failure model for inelastic composites with misaligned short fibers”. Composites Part A: Applied Science and Manufacturing, Vol. 42, I 12, pp 1892-1902, 2011.
[15] H. Herbst, Micro-mechanical modelling of heterogenous polypropylene compounds, PhD Thesis, University of Leoben, 2009, Leoben.
[16] Jerabek, M., Gastl, S., Major, Z., Herbst, H.: Characterization and Simulation of the Micromechanical Behavior of Particle Filled Polypropylene Compounds by DIGIMAT. DigiMat User Meeting, Bruxelles, Belgium (2008).
[17] Varga, Z. et al., 2006, Magnetic field sensitive functional elastomers with tuneable elastic modulus, Polymer 47, Elsevier, pp. 227-233.
[18] Varga Z, Filipcsei G, Zrínyi M. “Smart composites with controlled anisotropy”, Polymer, Vol. 46, pp. 7779-7787, 2005.
[19] Shen, Y. et al., 2004, Experimental Research and Modeling of Magnetorheological Elastomers, Journal of Intelligent Material Systems and Structures 15, SAGE, pp. 27-35.
[20] Kaleta J, Królewicz M, Lewandowski D. “Magnetomechanical properties of anisotropic and isotropic magnetorheological composites with thermoplastic elastomer matrices”, Smart Mater. Struct., Vol. 20, 085006, 2011.
[21] Hiptmair F, Major Z, Barroso V, Hild S, Wolfrum C. “Experimental Characterization of Magnetoelastomers and Determination of Material Model Parameters for Simulations”, APST 2 Conference proceedings, Linz, 2011.
[22] Hiptmair F, Major Z, Haßlacher R, Hild S, Schindler K, Wolfrum C. “Effect of Particle Surface Functionalities on the Mechanical Properties of Magnetoelastomers”, ASPM 2013 Conference proceedings, Bled, 2013.
[23] Major, Z., Schrittesser, B. and Filipcsei, G., 2009, Plastics, Rubber and Composites: Macromolecular Engineering, Vol. 38, No 8. 313-319.
[24] K. Haldar, A. Menzel, B. Kiefer, F. Hiptmair and Z Major, Constitutive Modeling of Magneto-viscous Polymers, PACAM XIV, 24-28 March 2014, Santiago, Chile.
[25] Filipcsei, G. et al., 2007, Oligomers, Polymer Composites, Molecular Imprinting: Magnetic Field-responsive Smart Polymer Composites, Advances in Polymer Science 206, Berlin: Springer, pp. 137–89.
[26] Reiter, M. and Major, Z., 2011, A combined experimental and simulation approach for modelling the mechanical behaviour of heterogeneous materials using rapid prototyped microcells, Virtual and Physical Prototyping, Volume 6, Issue, http://www.tandfonline.com/doi/abs/10.1080/17452759.2011.586949
[27] Haimin Yao, Huajian Gao, Multi-scale cohesive laws in hierarchical materials, International Journal of Solids and Structures 44 (2007) 8177–8193.
[28] S. Bekah, R. Rabiei, F. Barthelat, The Micromechanics of Biological and Biomimetic Staggered Composites, Journal of Bionic Engineering 9 (2012) 446–456.
[29] A. Kalteis and Z Major, Optimized Filler Particle Alignment and Stress Concentrations in Natural Objects, 10. Werkstoffkongress, 6-7 November 2013, Leoben
[30] http://industrial.panasonic.com/www-data/pdf/FAA3000/FAA3000CE1.pdf
[31] PolyUMod Library and the PolyUMod Manual, Veryst Engineering LCC, 2012.

Application of 2D-3D Surface Geometrical Features in Tribological Analysis of Ceramics and Ceramic Layers

Zsolt Maros[1, a], Csaba Felhő[1,b], Zoltán Vass[1,c] and Mária B. Maros[1,d]

[1]University of Miskolc, H-3515 Miskolc-Egyetemváros, Hungary

[a]zsolt.maros@uni-miskolc.hu (corresponding author), [b]csaba.felho@uni-miskolc.hu, [c]zoltan.vass@uni-miskolc.hu, [d]maria.maros@uni-miskolc.hu

Keywords: surface roughness parameters, wear, ceramic, ceramic layers

Abstract. Microgeometrical characteristics of the surface of engineering components operating in wear condition are important features influencing the wear process of the tribological system. Beside the widely used common 2D roughness parameters – e.g. the R_a, arithmetical mean roughness, R_z, ten point mean roughness, or R_{mr}, material ratio, etc. – the 3D roughness features (S_a, S_z S_{mr}) provide potentially new means for geometrical description of the operating surfaces. Our paper aims at contributing an overview on the available 2D and 3D features, giving their definition and their potential use in multi-scale characterization of components used especially in wear type loading conditions. An interesting question is the relationship between the 2D and 3D roughness parameters and their information content, relating to tribological problems. Besides giving a systematic overview of the most important parameters applicable in wear analyses we also present examples of 2D and 3D roughness data determined on surface of nitrocarburised steels, as well as silicon nitride ceramics. A special emphasis is placed on those parameters which can be most efficiently used during wear damage analyses of ceramic materials.

Introduction

The microgeometry of different parts can be characterized by a great number of roughness parameters. Unfortunately only a few parameters of them (e.g. arithmetical average roughness R_a, ten-point height R_z, etc.) are used in the machine industrial applications and these are describing the working properties of the actual surfaces not to the best [1, 2]. Nowadays the 3D topographical investigations are getting more and more common beside the 2D profilometrical applications at surface roughness examinations. These topographical examinations can provide data from the whole area of the surface and not only from one section of it, therefore represent significantly greater information.

The microgeometry of the surface has influence on the wearing properties of functional surfaces. If the relation between the microgeometry and the wear behaviour are going to be investigated, those roughness parameters should be used which characterize the wear performance to the best.

2D and 3D indexes of surface roughness

Roughness indexes (parameters) which are used to characterize the microgeometry of the surface can be classified into the following greater groups:

- amplitude parameters
- spacing parameters
- material ratio parameters
- functional parameters and
- hybrid parameters.

All of these indexes can be found both in 2D and in 3D investigations, and moreover most of them can be interpreted in the regards of roughness (R parameters), waviness (W parameters) and total profile error (P parameters) too.

Nowadays the application of amplitude parameters is general in profilometrical investigations:

- Maximum peak to valley height of the profile (R_t):
- Ten point height of the profile (R_z):
- Arithmetical mean deviation of the profile (R_a):
- Relative material ratio ($R_{mr(p)}$):

Using of 3D parameters is getting popular in the present days. Among that the application of the following ones is the most frequent [3, 4]:

- Material volume ratio (S_{mr})
- Maximum height of the surface (S_z):
- Arithmetical mean height of the surface (S_a):

Maximum height of the surface (S_z): It is the height between the highest peak and the deepest valley (Fig. 1) within the sampling area. It is calculated from the S_p (highest peak of the surface from the mean plane) and from the S_v (lowest valley of the surface from the mean plane). This parameter is corresponding to R_t value at profiles.

$$S_z = S_p + S_v \tag{1}$$

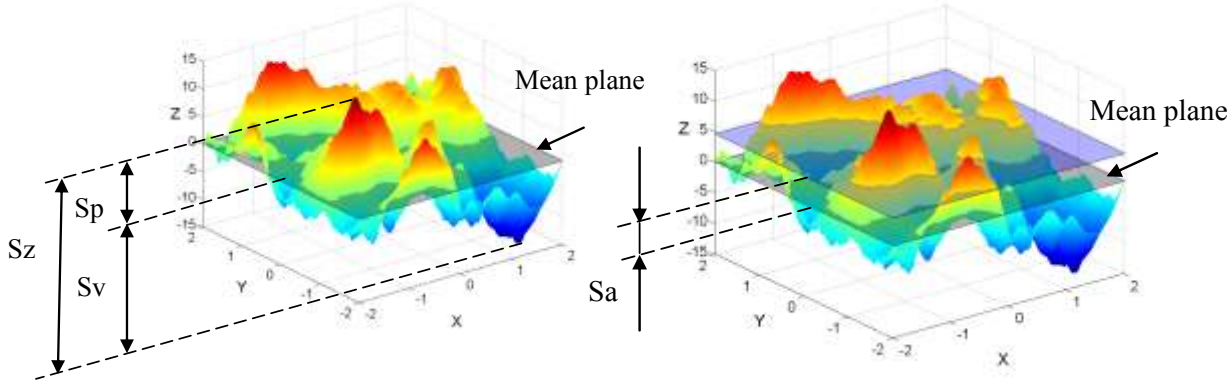

Figure 1: Calculation of the S_z and S_a parameter

Arithmetical mean height of the surface (S_a): It expresses the average of the absolute values of z(x,y) in the measured area (Fig. 1).

$$S_a = \frac{1}{A}\iint_A |z(x,y)|\,dxdy \tag{2}$$

This S_a value is corresponding to R_a but is evaluated on surfaces.

Problems of the common surface roughness indexes

Several parameters of surface roughness are not suitable to describe the working tribological surfaces. Consider the theoretical surfaces *a* and *b* in Fig. 2. From point of view of tribological characteristics the two surfaces are very different, however the commonly used 2D and 3D surface roughness indexes of them are absolutely equal in respect of parameters R_a, R_z, S_a or S_z. This obvious contradiction can be resolved if we use other surface roughness indexes for the characterisation of these surfaces. Such parameters could be e.g. the material ratio parameters (R_{mr}, S_{mr}) or the characteristic parameters of the Abbott-Firestone curve.

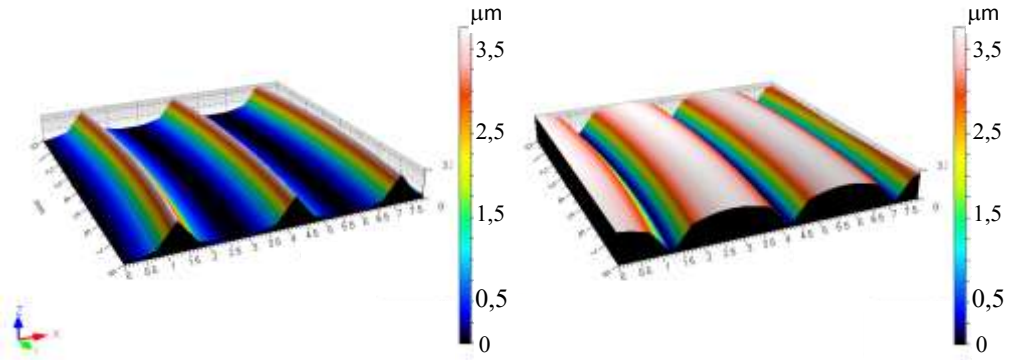

a) b)

Figure 2: Theoretical surfaces with different topography

Abbott-Firestone curves of the theoretically generated surfaces (a, b in Fig. 2) can be seen in Fig. 3, that shows clear differences between the two surfaces. This means, that the Abbott-Firestone parameters are more suitable to compare surfaces having different working characteristics.

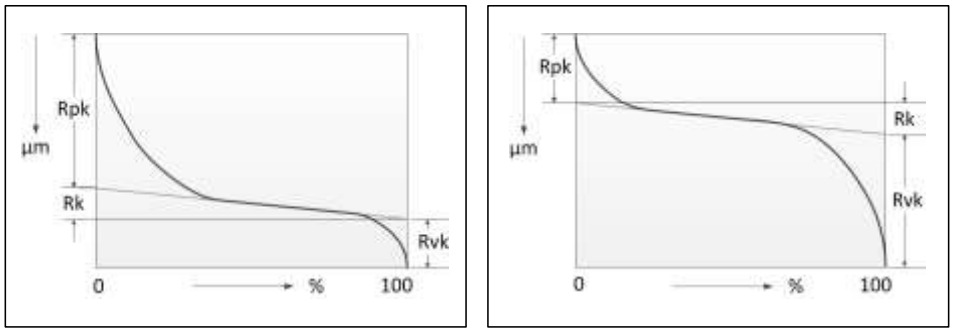

a) b)

Figure 3: Abbott-Firestone curves of theoretically generated surfaces (a, b)

From Fig 3. it is seen that – respecting the Abbott-Firestone parameters –surfaces *a* and *b* differ each other, thus these indexes are suitable for characterizing the working tribological surfaces.

Indexes of Abbott-Firestone (material ratio) curve

The material ratio curve (also called bearing ratio or Abbott-Firestone curve) gives the percentage value of the ratio of the material section to the whole section in a given depth from the highest peak. Red curves in Fig. 4. show material curves. In Fig. 4 the relative material ratio curve (blue columns) is indicated as well, this is some kind of density function from which the material ratio curve can be derived.

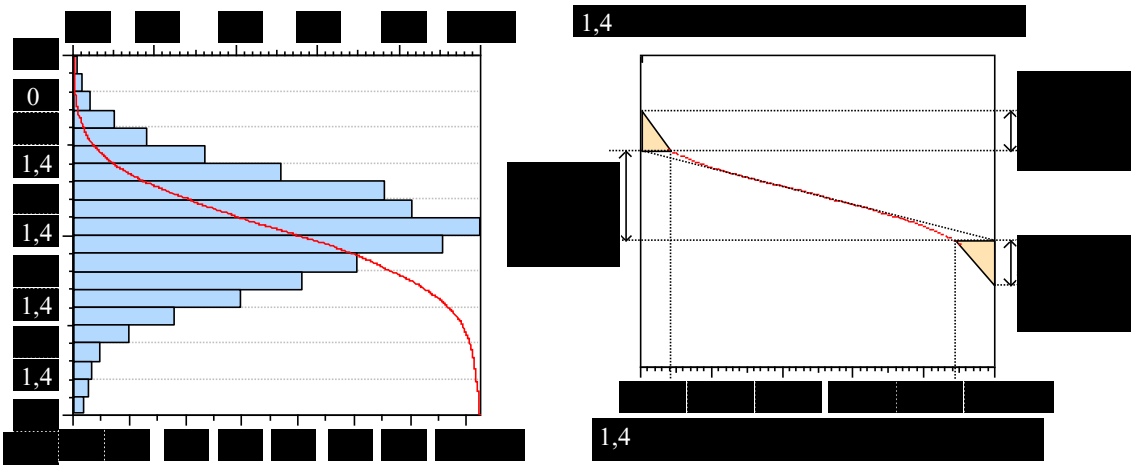

Figure 4: Typical Abbott-Firestone curves of working surfaces

Determination and meaning of parameters (R_{pk}, R_k and R_{vk}) of material ratio curves can be seen in Fig. 4. For tribological surfaces according to the literature

- R_{pk} is proportional to the amount of material that tends to worn down quickly,
- R_k related to the life time of the surface,
- R_{vk} indicates the oil retention and debris capability of the surface.

The corresponding three dimensional topography parameters are the S_{pk}, S_k and S_{vk}. These parameters give more reliable information about the working characteristics of the surfaces [5, 6].

Wear tests and investigation of surface roughness of nitrocarburised steels and Si_3N_4 nano-composites reinforced by graphene

Wear tests were carried out for the investigation of connection between the surface roughness and the wear characteristics of two nitrocarburised steel materials – 51CrV4 and 34CrMo4 – having ground and polished initial surfaces before the surface treatment.

Parameters of the ferritic nitrocarburising process were as follows:

- Gas composition: 250 l/h NH_3 + 10 l/h CO_2 + 50 l/h N_2;
- Temperature: T = 520°C and 570°C;
- Holding time: t = 8 and 16 h.

Si_3N_4 ceramic samples reinforced with different amount of graphene (0%, 1% and 3%) were sintered with different methods: Hot Isostatic Pressing (HIP) and Spark Plasma Sintering (SPS).

Pin-on-disc wear tests were carried out on UNMT-1 and UNMT-2 material testing equipments using the following test parameters:

	Nitrided steel	*Si_3N_4*
• loading force:	20 N	40 N
• ball diameter:	6,0 mm	5,93 mm
• ball material:	sapphire	SiC
• wear track radius:	3 mm	3 mm
• sliding speed:	100 mm/min	200 mm/min
• total wear length:	300 m	100 m

Results of the investigations

Surface topography of the probes was measured with AltiSurf 520 surface tester. 3D surface topography and the wear tracks can be seen in Fig. 5.

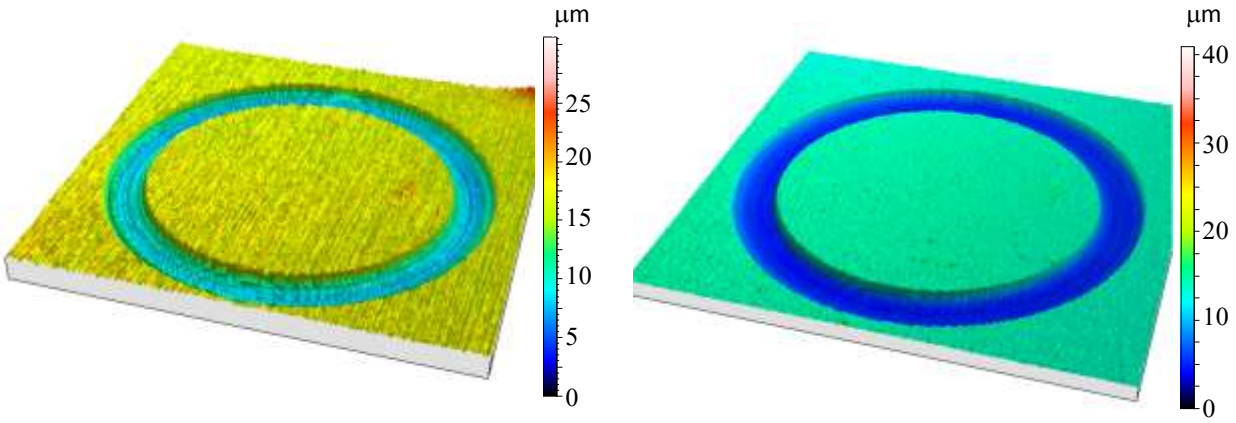

Figure 5: 3D topography and wear track of ground and polished nitrided 34CrMo4 steel probes

Worn cross sections of the wear tracks were measured with AltiSurf 520 surface profilometer.

Fig. 6. shows the extent of the worn cross section areas of nitrocarburised 34CrMo4 steel probes, having different initial surface topography (polished and ground). From Fig. 6. it can be established, that probes having the same treatment condition but different initial surface roughness show different wear characteristic. Based on this figure it can be seen that wear of the ground specimen is higher comparing to the polished one.

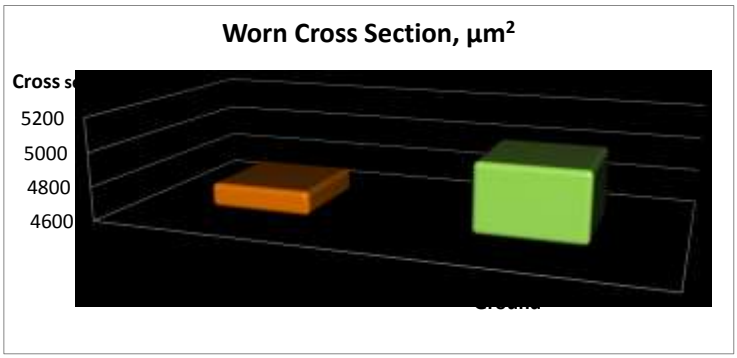

Figure 6: Worn cross sections of polished and ground nitrided 34CrMo4steel

Similar tendency can be recognised in Fig. 7. From this figure it can be seen that both 2D and 3D average surface roughness parameters and the Abbott-Firestone parameters show the same correlation as the worn cross sections.

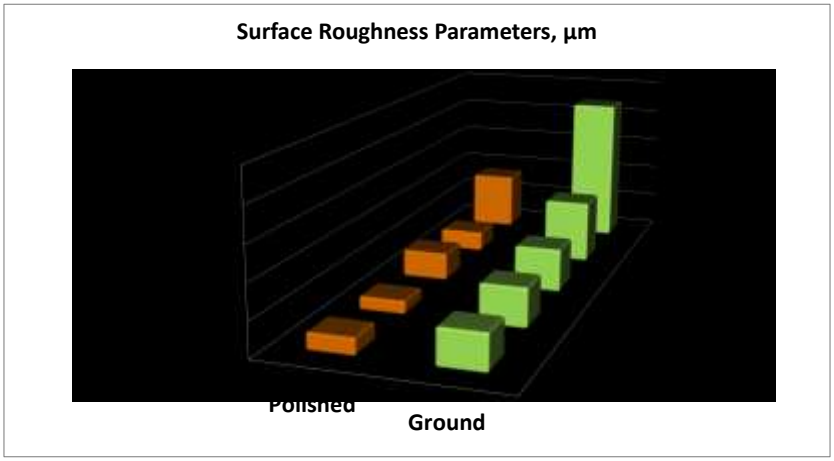

Figure 7: Worn cross sections of polished and ground nitrocarburised 34CrMo4steel

In case of Si_3N_4 samples containing graphene additive it can be recognised that wear of the specimens produced by HIP technology are higher in each case comparing to SPS specimens. In addition the worn cross section increases with increasing the graphene content (see Fig. 8).

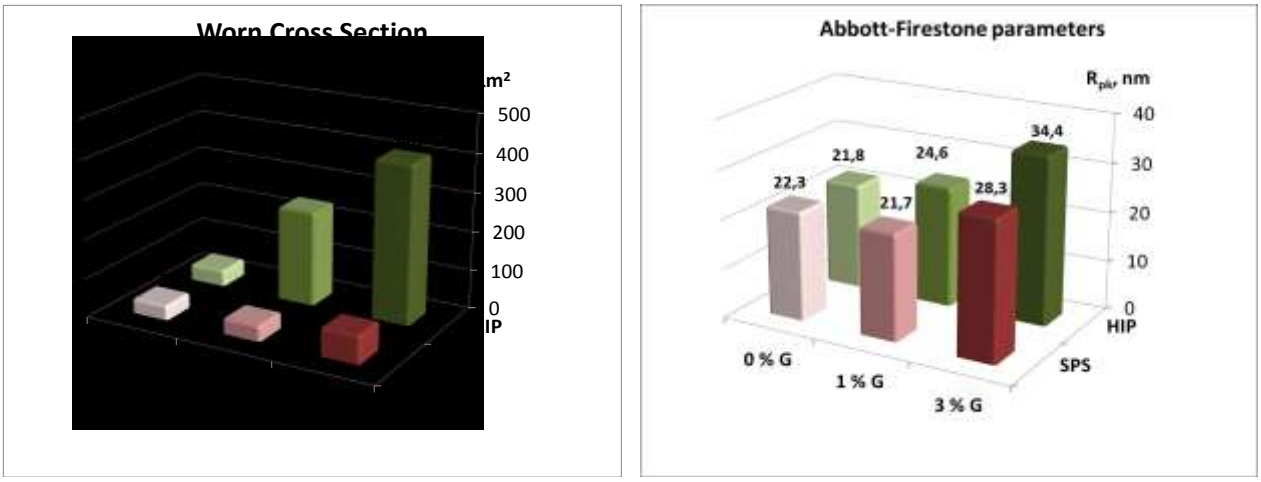

Figure 8: Worn cross section and R_{pk} roughness parameter of the graphene added Si_3N_4 samples

It can be seen from Fig. 8. that variation of the R_{pk} Abbott-Firestone parameter shows very good correlation with the change of the worn cross section in case of the different materials and production technologies. It means that in case of materials for which lower surface roughness can be reached applying the same production technology, the expected wear damage will be smaller as well.

Conclusions

Based on the executed experimental work and theoretical considerations the following conclusions can be drawn:

- Microgeometry (surface roughness) of contacting surfaces is an important influencing factor of the wear process.
- Selection of the proper surface roughness parameters should be done very carefully with special attention to the function of the operational surfaces.
- For the investigated nitrocarburised steel a connection between the worn cross section and the initial microgeometry of the surfaces could be revealed.
- During investigating the wear properties of the $Si3N_4$ ceramics reinforced with graphene, a connection between the worn cross section and the resistance to the abrasive manufacturing process (roughness after the polishing or grinding) could have been recognised.

Acknowledgement

The research work presented in this paper based on the results achieved within the TÁMOP-4.2.1.B-10/2/KONV-2010-0001 project and carried out as part of the TÁMOP-4.2.2/A-11/1-KONV-2012-0029 project in the framework of the New Széchenyi Plan. The realization of this project is supported by the European Union, and co-financed by the European Social Fund.

References

[1] Marko Sedlaček, Bojan Podgornik, Jože Vižintin: Correlation between standard roughness parameters skewness and kurtosis and tribological behaviour of contact surfaces, Tribology International, Volume 48, April 2012, Pages 102-112

[2] E.S. Gadelmawla, M.M. Koura, T.M.A. Maksoud, I.M. Elewa, H.H. Soliman: Roughness parameters, Journal of Materials Processing Technology, Volume 123, Issue 1, 10 April 2002, Pages 133-145.

[3] L. De Chiffre, S. Christiansen, S. Skade: Advantages and Industrial Applications of Three-Dimensional Surface Roughness Analysis, CIRP Annals - Manufacturing Technology, Volume 43, Issue 1, 1994, Pages 473-478

[4] N.K. Myshkin, A.Ya. Grigoriev, S.A. Chizhik, K.Y. Choi, M.I. Petrokovets: Surface roughness and texture analysis in microscale, Wear, Volume 254, Issue 10, July 2003, Pages 1001-1009

[5] S.F. Tian, L.T. Jiang, Q. Guo, G.H. Wu: Effect of surface roughness on tribological properties of TiB2/Al composites, Materials & Design, Volume 53, January 2014, Pages 129-136

[6] K.P. Shaha, Y.T. Pei, D. Martinez-Martinez, J.Th.M. De Hosson: Influence of hardness and roughness on the tribological performance of TiC/a-C nanocomposite coatings, Surface and Coatings Technology, Volume 205, Issue 7, 25 December 2010, Pages 2624-2632

Investigation of the data-requirement of ESTPHAD phase diagram calculation method

Tamás MENDE[1,a], András ROÓSZ[1,b]

[1]Hungarian Academy of Sciences, Materials Science Research Group, University of Miskolc 3515 Miskolc-Egyetemváros, HUNGARY

[2]University of Miskolc, Physical Metallurgy, Metalforming and Nanotechnology Institute, 3515 Miskolc-Egyetemváros, HUNGARY

[a]tamas.mende@uni-miskolc.hu, [b]femroosz@uni-miskolc.hu

Keywords: phase diagram, phase diagram calculation, ESTHPAD method, Al-Cu-Fe system

Abstract: The so-called phase diagram is one of the oldest but at the same time one of the most useful method for the material science. The role of algorithms and software calculating the phase diagram have an extraordinary importance in the industrial and research-development applications because remarkable advantages can be obtained by installing these software or the detailed and exact data base developed by them into either the simulation programs or into the everyday production (process-control, checking). In our present paper, the investigation of data-requirement of calculation method of ESTPHAD phase-diagram is described by processing binary- and ternary systems.

Introduction

Similar to the many different phase-diagram calculation methods (e.g. CALPHAD method [5][6][7]), the ESTPHAD phase-diagram calculation method having thermodynamic basis uses measurement data in the course of the calculations. The data-base consisting of concentration data pairs as for example the liquidus temperature necessary for performing the calculations is the most frequently developed by digitizing the curves and surface-isotherms of equilibrium phase diagrams existing in graphic form but the base of our calculations can also be the actual measurement data or the values obtained by other calculation methods of equilibrium phase diagram. However, it is really important to know the exact quantity of data necessary for performing the calculations and that how the change of quantity of data influence the exactness of calculation made by the ESTPHAD method. It can be very important to know the minimum size of data base when planning and compiling the alloy-series serving among others for measuring the liquidus temperature.

The Thermodynamic Basis of ESTPHAD Equation

In a binary alloy system, the free enthalpy of the regular liquid solutions as a function of concentration can be approximated as follows:

$$G = G_A c_A + G_B c_B + \Omega\ c_A c_B + RT(c_A \ln c_A + c_B \ln c_B) \quad (1)$$

Where: G - free enthalpy; Ω - interaction energy; c_A;c_B - concentrations of the phases; R - gas constant; T – temperature.

The partial molar free enthalpies are as follows:

$$\mu_A = G_A + \Omega\ (c_B)^2 + RT \ln c_A \quad (2)$$

$$\mu_B = G_B + \Omega\ (c_A)^2 + RT \ln c_B \quad (3)$$

Supposed that the binary system contains two phases (liquid and solid) which are in equilibrium, the equilibrium conditions can be written in the following way according to the Gibbs rule:

$$\mu_A^l = \mu_A^s \tag{4}$$

$$\mu_B^l = \mu_B^s \tag{5}$$

By taking into consideration the Gibbs rule, the equilibrium concentrations of phases (c_B^l, c_B^s), the distribution coefficient and the slope of liquidus temperature can be calculated at a given temperature from Equations 2 and 3 in case if the constants of Eq. 2 and 3 are known.

After a longer deduction and Taylor-series expansion [1], [2], the liquidus temperature can be calculated in the binary systems as follows:

$$T_l(c_B) = \frac{T_0}{1 + \sum_{i=1}^{n} A(i) \cdot c_B^i} = \frac{T_0}{1 + F_{AB}(c_B)} \tag{6}$$

Where: $T_l(c_B)$ - liquidus temperature; T_0 - melting point of the pure element; c_B - concentration of B element; $F_{AB}(c_B)$ - function calculated from the binary diagram; $A;B$ - the two components.

In case of a ternary system, the liquidus surface can be calculated similarly to the previous equation (Eq. 6), but it contains two binary polynomials ($F_{AB}(c_B)$; $F_{AC}(c_C)$) and a ternary polynomial ($\Delta F_{ABC}(c_B;c_C)$) which can be determined by a regression analysis (this type of equation can be called a hierarchical structure):

$$T_l(c_B) = \frac{T_0}{1 + F_{AB}(c_B) + F_{AC}(c_C) + \Delta F_{ABC}(c_B;c_C)} \tag{7}$$

Where: C - the third component; $\Delta F_{AB}(c_B)$ - function determined by regression analysis.

Investigation of the magnitude of data-base in case of binary systems

The following plan has been developed for determining the minimum quantity of data necessary for the ESTPHAD method.

1) The liquidus curves of equilibrium phase diagrams existing in graphic form have been digitized such a way that a concentration-temperature data pair having an order of magnitude of one hundred can be obtained. Then the A(i) parameters of ESTPHAD equation describing the given liquidus curve were determined by using the data base containing all the data moreover the differences between the digitized and calculated temperature-values were analyzed.
2) An „algorithm decreasing the data-base" was processed. *„m"* is the number of data digitized in point 1), *„k"* is the number of steps of decreasing and *„n"* is the quantity of data in the decreased data base which of course depends on *„k"*. (Naturally, in case of the whole data-base *m = n and k=0).* As a boundary condition, it was decided that the first and last values in the data base must not be deleted because in this case the validity area of determined ESTPHAD equation would decrease by losing these data as it would not cover entirely the composition-range of the original data base. It is necessary to decrease the data set between the first and last data points by uniform steps in order that the change of exactness of calculated data can be followed by decreasing the size of data base. The decrease by uniform steps was determined in the middle-point of data set between the two endpoints such a way that every second data shall be deleted and the first data to be deleted is the value following the first point of data base. The magnitude

of data base being present in the given step of „database in decreasing algorithm" can be calculated as follows:

$$n(k) = \frac{m-2}{2^k} + 2 \qquad (11)$$

3) The $A(i)_{n/m}$ parameters of ESTPHAD equation were determined from the *–„n(k)"* pieces of data-pairs at each of the data base developed in the different steps. The liquidus temperature was calculated and the exactness of calculations was analyzed by means of the calculated parameters for the whole data base (it means that at each *„m"* piece of digitized composition). The differences were compared with the calculation data obtained on the basis of the entire data base in the first step.

4) The data base was decreased until the difference between the digitized and calculated values remained within ±1 % as compared to the digitized temperature in case of all of *„m"* pieces of data by using the $A(i)_{n/m}$ parameters developed in the decreased data base. The quantity of data was not considered sufficient in case if the difference was greater than the aforementioned value at any point.

In the course of our investigations, the liquidus curve of phase rich in MgO of MgO-Al_2O_3 binary equilibrium phase diagram [3] was processed. The number of initial data was 188 and the quantity was decreased to 95, 48, 25, 13 and 7 data in accordance with the aforementioned system. The composition of data used in the calculation can be seen in Fig. 1. The liquidus curve was digitized at identical temperature steps from the beginning to the end (4.5 K) so fewer data could be obtained from the curve in the range with a lower Al_2O_3 concentration than in the further parts owing to the shape of liquidus curve (the slope of curve is less between 0-10% of Al_2O_3 content). It can be concluded from the aforementioned facts that in case of such liquidus curves having more complicated shapes, a database could be obtained which is not uniform as far as the data-distribution is concerned owing to the data-decrease by decreasing every second data; less data are available about the certain parts of curve (in our case about its beginning). By analyzing the difference between the digitized and calculated values during the investigations of decreased data-base it can be stated that the greatest differences of the whole calculation (having an acceptable range even in this case) appear in this Al_2O_3 range of 0-10%. It is due on the one hand to the fact that this part of curve-shape can be matched in a more complicated way and on the other hand that the data are missing.

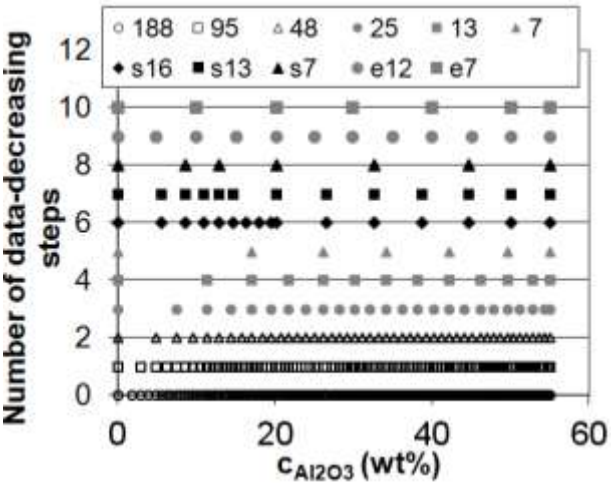

Fig. 1: Steps of decreasing the data-base. Data-base decreased by bisection, decreased in a weighted way as well as decreased uniformly from the point of view of concentration

Essentially, the values of temperature data are uniformly decreased by deleting every second data. However, an investigation during which the data were decreased by a uniform distribution from the point of view of concentration was also performed, data by 5 mass% (Al_2O_3) then by 10 mass% were used in the calculation (e12, e7 data-series in Fig. 1). As we have already mentioned, the shape of liquidus curve changes essentially between 0-10% of Al_2O_3 content; it shows a tendency decreasing by a relatively uniform slope in the further part. It was also investigated if the higher difference experienced at the beginning of curve during starting our investigations could be decreased in case if more data are used in the course of our calculations from the range of varying slope i.e. if this curve section was weighted (s16, s13, s7 data-series in Fig. 1).

By means of the ESTPHAD function developed by using all of the different quantities of data, the liquidus temperature was calculated in all the 188 points; the difference between the digitized and calculated values can be seen in Fig. 2. In part (a) the calculations of data bases decreased by bisection, in part (b) the results of data bases decreased in a weighted way and decreased uniformly from the point of view of the composition can be seen.

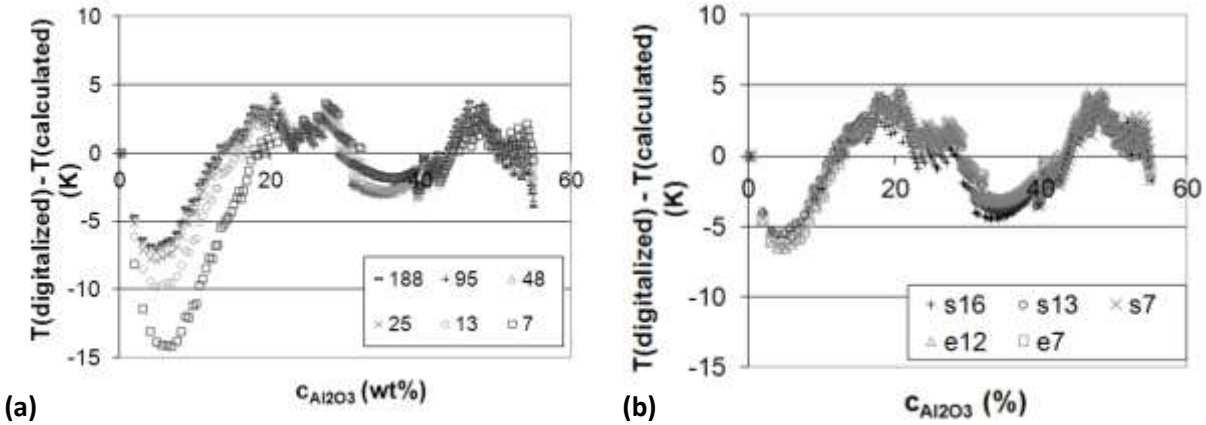

Fig. 2: The difference between the digitized and calculated data as a function of SiO_2 concentration in case of data-bases decreased by bisection (a) and in case of data-bases decreased in a weighted way as well as by the steps of uniform composition (b). (Phase rich in MgO, Mgo-Al_2O_3 system).

By knowing the differences (the difference is less than 0.5% as compared to the digitalized temperature) it can be stated that the liquidus curve of MgO phase can be described by a suitable exactness by using 6-7 measured (digitized) data by means of the ESTPHAD method. The difference is max. 0.21% of the digitized temperature even in case of using 7 data in case if the more complicated part of curve is used in the calculations in a weighted way or the data base has a uniform concentration distribution (e.g. one measured data is 10%/Al_2O_3) and so no one of the parts of curves is missing from the process of polynomial-matching.
In (a) part of Fig. 3, the change of average differences can be seen as a function of the quantity of data used during the calculation of temperature. Initiating from 188 data, the median decrease can be seen moreover the results of decrease performed in a weighted was as well as of the decrease following the uniform concentration distribution can be seen in case if the number of data is less than 20 (the differences can be seen among the three different methods). In part (b), the liquidus curves calculated on the basis of data-bases decreased by bisection; it can be observed that even the 7-data matching showing the greatest average difference does not differ significantly from the other curves.

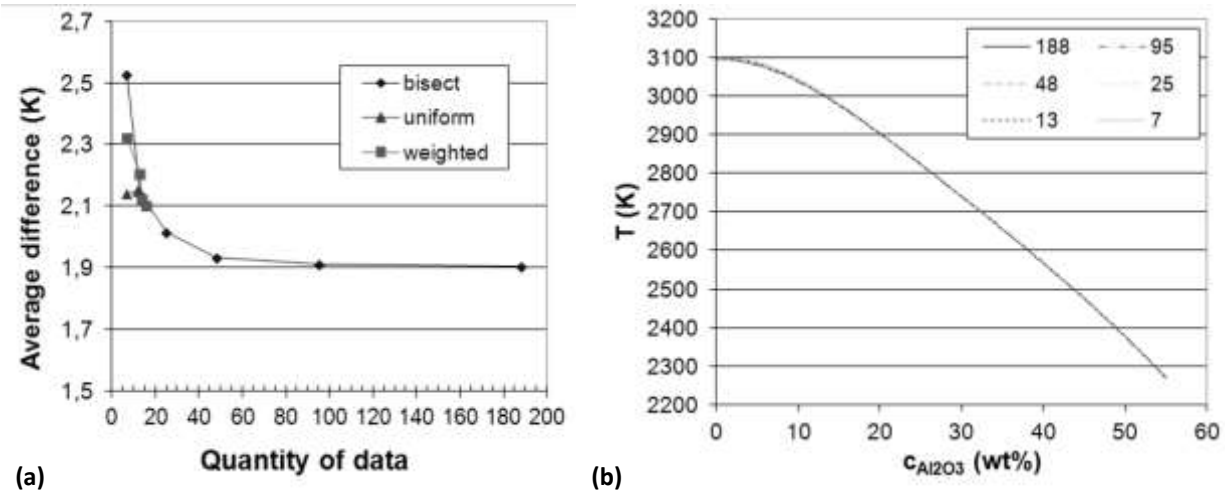

Fig. 3. (a) The average difference of digitized and calculated data as a function of the quantity of data used during the calculations. (b) Liquidus curves calculated by using the A(i) parameters obtained at different quantities of data (phase rich in MgO, MgO-Al_2O_3 system)

Investigation of the magnitude of data base in case of ternary systems

The liquidus surface of α phase rich in Al [4][8] was processed in order to investigate the data-requirement of calculations of ternary systems of ESTPHAD method. The isotherms of liquidus surface were digitized by a high quantity of data (it was not necessary to use an initial quantity of data of an order of magnitude of 100 on the basis of the results of binary system) then the quantity of data was decreased gradually in more steps. Similar to the binary investigations, the parameters of ESTPHAD equation were calculated at each decrease then the differences were analyzed for the whole data-base. The decreases were performed such a way that the melting point of pure Al as well as the peripheral data of isotherms were kept and the intermediate values were decreased. At last the decreased quantity of data indicated by circles in part (a) of Fig. 4 was obtained from the digitized data indicated by points in part (a) of Fig. 4. An investigation during which the decreased quantity of data was obtained in the last step such a way that an entire isotherm was taken out of the system was also performed (part (b) in Fig. 4).

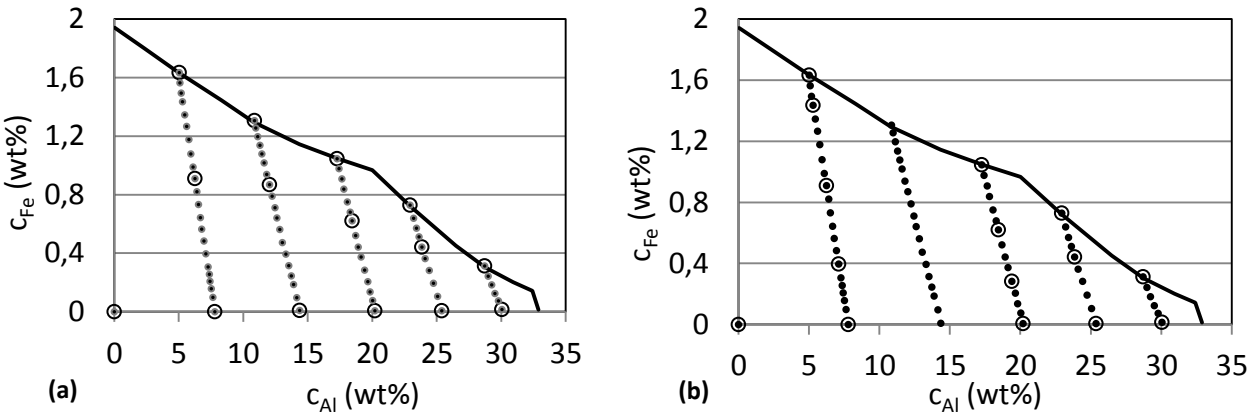

Fig. 4: (a) Data-base decreased uniformly and **(b)** data-base decreased by isotherm in case of the liquidus surface of α phase of Al-Cu-Fe system

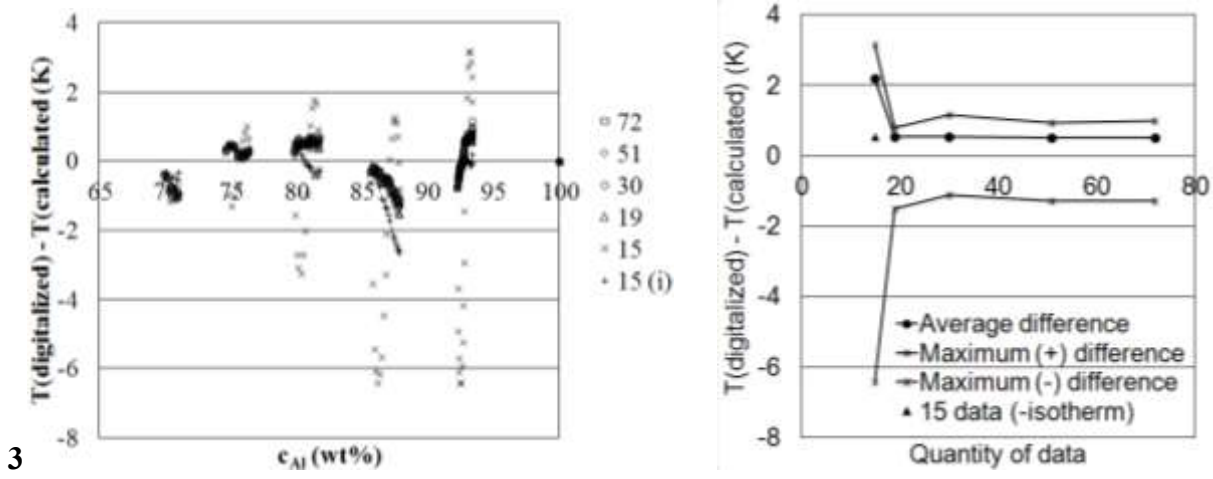

Fig. 5. (a) Differences between the values of liquidus temperatures calculated during the digitized [4] and decreased data bases and **(b)** the values of the average- and highest differences as a function of the value of data base in case of the liquidus surface of α phase of Al-Cu-Fe system

In Figs 5 (a) and (b) it can be seen that the liquidus temperature can be calculated by an approximately identical exactness by decreasing the quantity of data to 19 data as if a data base of wide range was processed. If the quantity of data is less than the aforementioned quantity (15 data), the differences become higher but even in this case, the differences are under ±1% as compared to

the values of digitized liquidus temperature. The values of differences follow the previous extent in case if one isotherm is missed but we have got more data about the existing isotherms (i.e. the overall quantity of data is constant – 15 pieces). 6-9 calculated parameters are used for the exact description of liquidus surfaces in the ESTPHAD method. Consequently, it can be stated that the liquidus surface of ternary systems can be described in an order of magnitude by a suitable exactness by using data the quantity of which is twice more than the number of applied parameters.

Conclusions

The data-requirement of ESTPHAD method for calculating the phase diagram was investigated in case of binary- and ternary systems. On the basis of the results of investigations, it can be stated that it is not necessary to record a lot of data-points in order to describe a liquidus curve/surface but it is enough to determine the liquidus temperature at 6-7 compositions in the binary systems and at 15-18 compositions in the ternary systems (having a suitably representative concentration distribution) without the essential deterioration of the results. In general it can be stated that the quantity of necessary measurement data-base is twice more than the number of polynomial parameters in the ESTPHAD equation used for the description of curve/surface.

Acknowledgement

This research was supported by the European Union and the State of Hungary, co-financed by the European Social Fund in the framework of TÁMOP 4.2.4. A/2-11-1-2012-0001 'National Excellence Program'. *(Tamás MENDE)*

The research work presented in this paper based on the results achieved within the TÁMOP-4.2.1.B-10/2/KONV-2010-0001 project and carried out as part of the TÁMOP-4.2.2.A-11/1/KONV-2012-0019 project in the framework of the New Széchenyi Plan. The realization of this project is supported by the European Union, and co-financed by the European Social Fund." *(András ROÓSZ)*

References:

[1] A. Roósz, G. Kaptay, J. Farkas, Thermodynamics-Based Semi Empirical Description of Liquidus Surface and Partition Coefficients in Ternary Al-Mg-Si Alloy, Materials Science Forum, 414-415 (2003) pp. 323-328

[2] T. Mende, A. Roósz: Calculation of the Immiscibility Gap by ESTPHAD Method, Materials Science Forum, 659 (2010) pp. 423-428

[3] Muan, Arnulf, Osborn: Phase Equilibria Among Oxides in Steelmaking, Pergamon Pr., 1965

[4] Equilibrium Diagrams of Aluminium Alloy System, The Aluminium Development Association, London (1961)

[5] Dezső András, Kaptay György: Rézforrasztásra használt ón-ezüst réz rendszer egyensúlyi vizsgálata, Országos Magyar Bányászati Egyesület, BKL Kohászat, 147. (2014), pp. 2-6.

[6] Ales Kroupa: Modelling of phase diagrams and thermodynamic properties using Calphad method – Development of thermodynamic databases, Computational Materials Science, Volume 66, January 2013, pp. 3-13

[7] Jimmy Gran, Yanli Wang, Du Sichen: Experimental determination of the liquidus in the high basicity region in the Al2O3(30 mass%) - CaO - MgO - SiO2 system, Calphad, Volume 35, Issue 2, June 2011, pp. 249-254

[8] A. Waseda, K. Kimura, H. Ino: Free energy analysis for the phase transition of quasi-crystals and phase diagram of the Al-Cu-Fe system, Materials Science and Engineering: A, Volumes 181–182, 15 May 1994, pp. 762-765

Determination of dislocation density in cubic systems

Péter J. Szabó[a], András Csóré[b]
Department of Materials Science and Engineering, Faculty of Mechanical Engineering,
Budapest University of Technology and Economics
Bertalan L. u. 7., H-1111 Budapest, Hungary
[a]szpj@eik.bme.hu, [b]ram92@freemail.hu,

Keywords: quasi-dislocation density, SEM, EBSD, misorientation, Nye-tensor, austenitic steel, measuring software, C#

Abstract. From the lattice orientation of a sample, elements of the Nye-tensor can be determined. With the help of Nye's tensor, dislocation density can be calculated for the certain sample. Since the measures were carried out with scanning electronmicroscope (SEM), just superficial orientations can be measured. Hence the Nye-tensor is an incomplete matrix, with five elements. Because of the absence of the other four elements just a quasi-dislocation density can be obtained. The algorithm of the calculation was programmed on the language C#.

Introduction

Nowadays metals are widely used materials. The strongest magnets or structural materials as well as conducting cables are made of metals and alloys, but many other applications can be mentioned. Therefore, it is very important to have information about physical (e.g. mechanical, optical, conduction) properties. These features do not only depend on chemical composition, but are highly influenced by the lattice and the grain structure.

In practice, lattice structures have defects in every case. Lattice defects can be divided into four groups according to their spatiality: pointlike, linear, superficial, spatial. Mechanical properties (elasticity, etc.) are highly influenced by one-dimensional defects called dislocations. Let a perfect crystal be considered. If a part of the crystal is shifted along a plane or a semiplane (slideplane), the lattice will be deformed and tension will appear. The shifted and non-shifted part of the lattice are separated by the dislocation line which is a one-dimensional domain. Dislocations can be catalogued into three groups: edge dislocation, screwed dislocation, and mixed dislocation. Considering mechanical properties, not the type, but the amount of dislocations does matter.

Crystal orientation is defined as the directionality of the Cartesian coordinate system fitted on a part of the lattice. The position of this coordinate system is compared to a reference Cartesian system which is fixed to the sample being examined. It is can be clearly seen, that orientation changes are eventuated by dislocations. (Although orientation changes are also caused by superficial and spatial defects, due to a certain condition they can be eliminated during the calculation.) The measuring technique - worked out during the research – is based on this correlation between crystal orientation and dislocations: the amount of dislocations can be determined from the inner metallic orientation changes.

The orientation of each points contained by the sample can be determined with the help of the EBSD (Electron BackScattering Diffraction) function of a scanning electronmicroscope (SEM). It is very important to note, that the scanning of the surface is not continuous. In other words: with SEM only the orientation of discrete superficial points (with an adjustable measuring step, i.e. resolution) can be measured; and spatial scanning cannot be carried out.

Inter alia, the Euler angles between the coordinate system of each points and the reference system are contained by a database obtained by the software of the microscope. Using these data, the so-called Nye dislocation density tensor referred to one point can be obtained with the help of a mathematical algorithm. For the whole sample it can be obtained by averaging.

Hundreds or thousands of points is being examined during one measuring. It is impossible to evaluate manually, thus a code have been written in the language C#. Due to this program, Nye tensor can be determined easily from the database containing the Euler angles.

Method

A metallic sample – after adequate preparation – can be examined with the help of a SEM with the EBSD function mentioned above. In determined points on the surface of the sample, lattice orientation can be measured, and the Euler angles can be obtained. Naturally, one point does not have orientation, but the electron beam emitted by the cathode has finite cross-section, therefore the "point" being examined is not literally a point, but a domain. In this domain lattice orientation is assumed to be the same. The measuring points are placed on a square grid.

The file which contains the Euler angles and Cartesian coordinates of the points in the reference system (on the square grid in x-, y-directions) is read by the program written in C#. From the Euler angles and the position of the points the Nye-tensor – mentioned in the Introduction - can be calculated with a mathemathical algorithm. Henceforward this algorithm will be reviewed.

Let ϕ_1; ϕ_2; and φ be the Euler angles of the i-th point on the surface of the sample being examined. Then the so-called Bunge orientation tensor denoted with **G** can be obtained for each point [4] with Eq. 1.

$$\boldsymbol{G} = \begin{bmatrix} \cos\varphi_1 \cos\varphi_2 - \sin\varphi_1 \sin\varphi_2 \cos\phi & \sin\varphi_1 \cos\varphi_2 + \cos\varphi_1 \sin\varphi_2 \cos\phi & \sin\varphi_2 \sin\phi \\ -\cos\varphi_1 \sin\varphi_2 - \sin\varphi_1 \cos\varphi_2 \cos\phi & -\sin\varphi_1 \sin\varphi_2 + \cos\varphi_1 \cos\varphi_2 \cos\phi & \cos\varphi_2 \sin\phi \\ \sin\varphi_1 \sin\phi & -\cos\varphi_1 \sin\phi & \cos\phi \end{bmatrix} \quad (1)$$

Assuming that misorientation between two adjacent points caused by the dislocations between them, a mathemathical object is needed for characterizing the degree of the misorientation. This object is the misorientation tensor - denoted with **M** – and can be obtained with the following equation [3]

$$\mathbf{M_i} = \mathbf{G_A G_B^{-1} C_i}, \quad (2)$$

where **G** matrices are the orientation matrices of two neighboring points indexed with A and B. The $\mathbf{C_i}$ matrices are the symmetry matrices. (In cubic systems there are 24 of them [3].) Henceforward quaternionic representation will be used [1], because of the simpler usage. In this representation, the orientation of a point (Eq. 3) and the misorientation (Eq. 4) of two neighboring points can be seen below.

$$q_0 = \frac{1}{2}\sqrt{\boldsymbol{G}_{ii} + 1}\,; \qquad q_i = -\frac{\varepsilon_{ijk}\,\boldsymbol{G}_{jk}}{4q_0} \quad (3)$$

$$\mathbf{q_A q_B^{-1}} = \mathbf{\Delta q} \quad (4)$$

As it mentioned above, there are many misorientation matrices - such as **Δq** quantities - can be obtained between two points. That **Δq** quantity will be the chosen one, which belongs to the minimal misorientation angle denoted with Θ, and can be calculated with Eq. 5 [1].

$$\Theta = 2\arccos(\Delta q_0) \tag{5}$$

Then the values of the **Δq** for each first-neighbored measuring point separately for the x- and y-directions will be averaged. With the help of these average values the elements of the Nye-tensor (Eq. 6) can be easily calculated with Eq. 7 [2].

$$\boldsymbol{\alpha} = \begin{bmatrix} \alpha_{11} & \alpha_{12} & \alpha_{13} \\ \alpha_{21} & \alpha_{22} & \alpha_{23} \\ \alpha_{31} & \alpha_{32} & \alpha_{33} \end{bmatrix} \tag{6}$$

$$\alpha_{lk} = \Delta q_k \frac{2\arccos(\Delta q_0)}{\sqrt{1-\Delta q_0^2}} \frac{1}{\Delta x_l} \tag{7}$$

In Eq. 7 the step size in the separate directions denoted with x_l. (Since the measuring points are fitted in a square grid, the value of x_l will be the same for the x direction as well as the y direction.)

It can be clearly seen that not all of the elements can be obtained because with SEM spatial examination cannot be carried out. Thus a so-called quasi-dislocation density can be obtained, with

$$\rho^* = \frac{1}{b}(|\alpha_{12}| + |\alpha_{13}| + |\alpha_{21}| + |\alpha_{23}| + |\alpha_{33}|), \tag{8}$$

where b is the length of the Burgers-vector and ρ* is the quasi-dislocation density [1].

As it mentioned above, a measuring software have been created. The input is the .txt file obtained by the software of the SEM, the output is the obtainable elements of the Nye-tensor and the quasi-dislocation density.

Results

The software – carried out during our research – was tested on two FCC (Face Centered Cubic) samples, which went through different kinds of plastic-forming methods.

Comparison of annealed and caliber-rolled austenitic steel samples

The first test was performed on austenitic steel samples. One of the samples was long-time annealed, the other was caliber-rolled and heat-treated for ten minutes. On each sample two different parts were chosen and measured using SEM. During the evaluation for the value of the Burgers-vector $|\underline{\mathbf{b}}| = 2.51 \cdot 10^{-10}$ m was set. Each measure was carried out with square technique. The step size was 6 μm. Quasi-dislocation density data can be seen in Table 1.

Data of austenitic steel samples

Quasi-dislocation density [1/m^2]		
Number of the sample	Annealed	Formed
1	2,13E+13	8,79E+13
2	3,54E+13	3,05E+14

Table 1

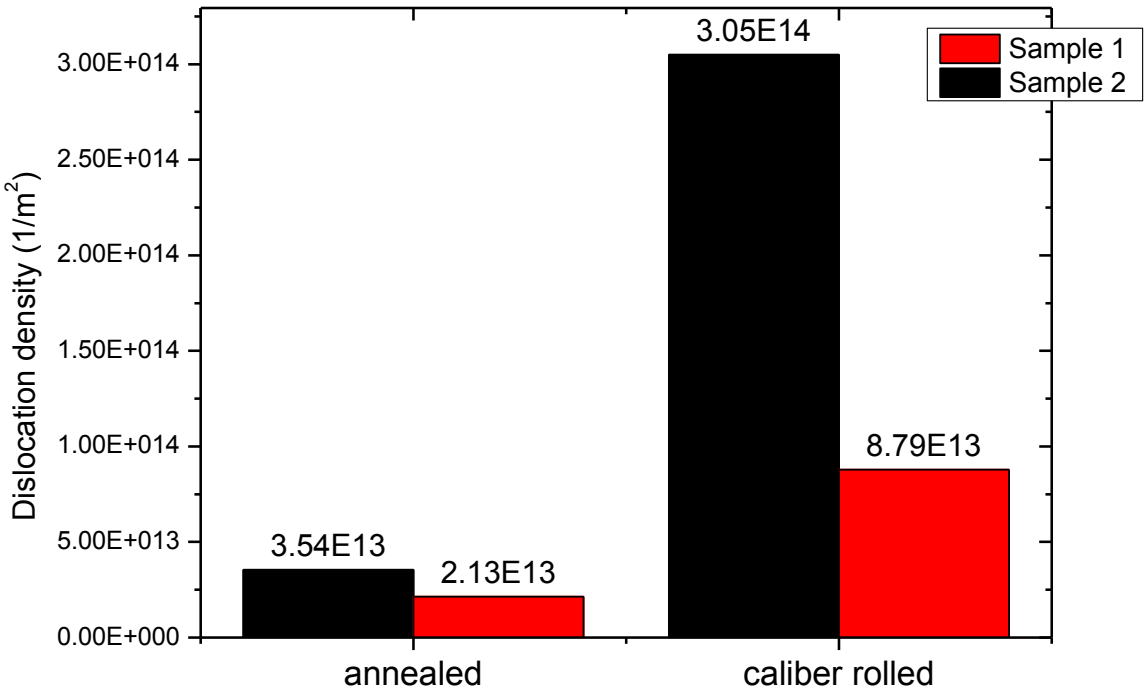

Fig. 1
Dislocation-density in annealed and caliber rolled austenitic steel

Based on Table 1. and Fig. 1, it can be determined that the values given by the software are such as expected: in the caliber-rolled sample there is a higher value of dislocation density. It is very important to note, that these values are just relatively reliable. Much more tests are needed to make conclusions about the values absolutely.

Summary

From the lattice orientation dislocation density can be calculated. Dislocation density can be obtained from Nye's tensor which is an incomplete matrix. This matrix has five elements. The other four cannot be obtained because the measures were carried out just on the surface of the certain sample with the help of scanning electronmicroscope. Hence just a quasi-dislocation density can be obtained. Since, on the surface of the sample there are hundreds, thousands or even more measuring points, the algorithm of the calculation was programmed in the language C#. The input is the database obtained by the software of the SEM and the Burgers-vector; the outputs are the elements of the Nye tensor, and the quasi-dislocation density. The operation of

the program was tested with annealed and caliber-rolled austenitic steel samples. (Tests were carried out with the database of other samples too, e.g. annealed and equal-channel angular pressed copper.) According to our results, we can say that the samples, relative to each other have the expected dislocation density values. For further conclusions (e.g. choosing the right resolution, reliability of the dislocation density values) more tests are needed.

References

[1] W. He, W. Ma, W. Pantleon, *Microstructure of individual grains in cold-rolled aluminium from orientation inhomogeneities resolved by electron backscattering diffraction*, Materials Science and Engineering A 494 (2008) 21–27

[2] W. Pantleon, *Resolving the geometrically necessary dislocation content by conventional electron backscattering diffraction,* Scripta Materiala 58 (2008) 994-997

[3] Hiromoto Kitahara, Rintaro Ueji, Masato Ueda, Nobuhiro Tsuji, Yoristoshi Minamino, *Crystallographic analysis of plate martensite in FE-28.5 at.% Ni by FE-SEM/EBSD*, Materials Characterization 54 (2005) 378-386

[4] H.-J. Bunge, *Texture Analysis in Materials Science: Mathematical Methods*, Cuvillier Verlag, Göttingen, 1993, pp. 1–19.

Determination of Flow Curve by Cylindrical Upsetting Based on the Principle of Virtual Power

Viktor Szombathelyi[1,2,a,*], György Krállics[2,b], Péter Rózsahegyi[3,c]

[1] College of Dunaújváros, Department of Material Science, H-2400, Táncsics M. str. 1/A, Dunaújváros, Hungary

[2] Budapest University of Technology and Economics, Department of Material Science and Engineering, H-1111, Bertalan L. str. 7, Budapest, Hungary

[3] Bay Zoltán Nonprofit Ltd. for Applied Research, H-1116, Fehérvári út 130, Budapest, Hungary

[a] szombathelyi@mail.duf.hu [b] krallics@eik.bme.hu [c] rozsahegyi.peter@bay-logi.hu

Keywords: flow curve, cylindrical upsetting, barrelling, principle of virtual work.

Abstract. In the design of metalworking technologies, one of the most important amount is the flow stress of the material. A few experimental method can be used to measure it. The most commonly used tests to determine the flow curve of materials include upsetting of cylindrical or prismatic specimens, tension or torsion tests. In our work, the determination method of flow curve were investigated based on the principle of virtual power with cold working conditions. The experimental method, cylindrical upsetting, was executed on the Gleeble 3800 thermo-mechanical simulator. The goal was to determine reliable flow curve for large plastic strain. The results showed that reliable flow stress values were obtainable in equivalent plastic strain range of 0 to 0.7 by continuous cylindrical upsetting.

Introduction

A number of simple mechanical tests can be used for measuring the flow curve. In all cases, a kind of specific stress state in the whole volume are desired. Under large strain the geometry of the deforming sample is distorted, the initially homogeneous state of strains and stresses become inhomogeneous. There are two widely used methods, in case of cylindrical upsetting, to reduce the effect of friction. In one case, the friction reduced by high viscosity lubricant placed between the tool and the specimens [1]. In the other case shape correction is used to eliminate the effect of friction [2,3]. The plane strain compression test, otherwise known as Watts-Ford test, gives the best approximation for the flow curve [4]. In this test to minimize the effect of friction, the specimens are re-lubricated at each compression step; and to keep the plane strain state a determined tool and specimen geometry are required. In our work, the calculated flow stress results are compared to the results obtained by Watts-Ford method.

Mechanical model

A mechanical model was developed using the data from the simulations. The model is based on the following fundamentals. During the compression the maximum diameter and the actual height are measured. There are two approximation to describe the contour of the deformed specimen. In this model, parabolic approximation is used. The geometry of the specimen at the initial and the deformed state are shown in Fig. 1.

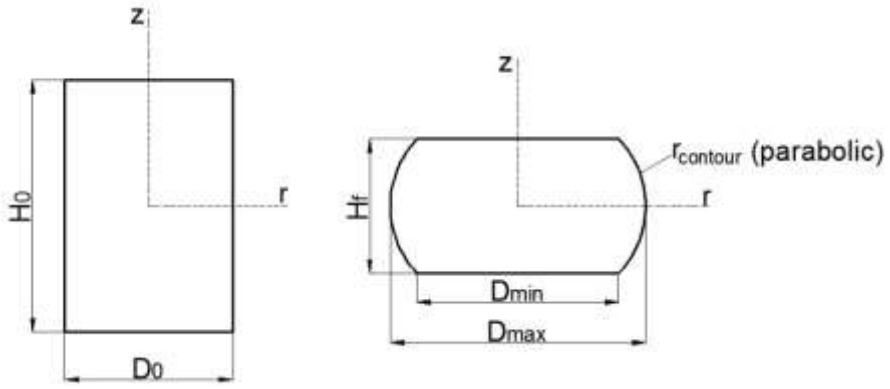

Fig. 1 The geometry of the specimen at the initial (left) and the final state (right)

Applying the principle of virtual power, the functional of plasticity has to be determined at its stationary point, which gives the actual one among all the kinematically admissible velocity field $\mathbf{v}$. The material is assumed to isotropic and incompressible and the inertia forces are suppressed [5].

$$J = \iiint_{V_p} I dV + \iint_{A_\tau} \boldsymbol{\tau}^* \Delta \mathbf{v}_\tau dA + \iint_{A_\Delta} \boldsymbol{\tau}_\Delta \Delta \mathbf{v}_\Delta dA - \iint_{A_\sigma} \mathbf{t}^* \mathbf{v} dA - \mathbf{Q}^* \mathbf{v}_{rigid}$$
$$\delta J = 0 \tag{1}$$

The first term expresses the internal power over the deformed volume V_p, where $I = \int_0^{\bar{\xi}} k_f(\bar{\xi}) d\bar{\xi}$ is the power of the plastic deformation over a unit volume, where k_f is the flow stress, $\bar{\xi}$ is the equivalent plastic strain. The second term covers the frictional power on the contact surface A_τ, where $\boldsymbol{\tau}^*$ is the shear stress vector, $\Delta \mathbf{v}_\tau$ is the relative velocity vector between the anvil and the workpiece. The third term defines the shear power over the surface of velocity discontinuities A_Δ, where $\boldsymbol{\tau}_\Delta$ is the shear losses vector on surfaces of velocity discontinuities, $\Delta \mathbf{v}_\Delta$ is the velocity discontinuity vector. The fourth term represents the power of the $\mathbf{t}^*$ stress vectors acting on surface A_σ. The last term is the external power, where $\mathbf{Q}^*$ is the external force vector acting on the rigid body, which is connected to the deformation zone and $\mathbf{v}_{rigid}$ is the velocity vector of the rigid body. The variation of this functional is zero at its stationary point. In the case of cylindrical upsetting the third, fourth and fifth term are equal to zero. The Eq. 1 becomes

$$J = \iiint_{V_p} I dV + \iint_{A_\tau} \boldsymbol{\tau}^* \Delta \mathbf{v}_\tau dA \tag{2}$$

Velocity field and strain rate tensor field. The radial component of the velocity field, taking account the barrelling effect, is obtained as

$$v_r = \frac{1}{2}\xi_0 r + r\left(a_1 + a_2 \frac{r^2}{R_{\max}^2}\right)\left(1 - 3\frac{z^2}{h^2}\right) \tag{3}$$

where a_1, a_2 are the variational parameters, R_{max} the maximum radius, h the height at a given state and $\xi_0 = -\frac{v}{h}$. Taking into account the volume constancy the components of the strain rate tensor are

$$\xi_{rr}=\frac{\partial v_r}{\partial r};\quad \xi_{\theta\theta}=\frac{v_r}{r};\quad \xi_{zz}=-\left(\xi_{rr}+\xi_{\theta\theta}\right);\quad \xi_{rz}=\frac{1}{2}\left(\frac{\partial v_z}{\partial r}+\frac{\partial v_r}{\partial z}\right);\quad \xi_{r\theta}=\xi_{\theta z}=0 \tag{4}$$

The equivalent plastic strain rate is obtained as follows:

$$\bar{\xi}=\frac{\sqrt{2}}{3}\sqrt{\left(\xi_{xx}-\xi_{yy}\right)^2+\left(\xi_{xx}-\xi_{zz}\right)^2+\left(\xi_{zz}-\xi_{yy}\right)^2} \tag{5}$$

The calculation of the equivalent plastic strain, because of the inhomogeneous state of strain, is difficult. In case of low friction factor value the average equivalent plastic strain, characterized the whole deformed volume, is calculated as:

$$\bar{\varepsilon}=2\ln\left(\frac{H_0}{H_f}\right) \tag{6}$$

where H_f and H_0 are the maximum and initial height, respectively.

Internal power of deformation. The internal power of deformation is

$$\dot{W}_i=\int_0^h\int_0^{r_{contour}} 2\pi r k_f\bar{\xi}\,dr dz \tag{7}$$

where k_f is the flow stress and $r_{contour}$ is the contour of the specimen assuming parabolic approximation.

$$r_{contour}=r_{\max}+\frac{\left(r_{\min}-r_{\max}\right)}{h^2}z^2 \tag{8}$$

where r_{min} is the minimum radius, calculated from the volume constancy.

Frictional power. The frictional power is obtained as:

$$\dot{W}_\tau=\int\!\!\int_{A_\tau}\tau\,\Delta v_\tau\,dA \tag{9}$$

where, according to the constant shear assumption $\tau^*=m\frac{k_f}{\sqrt{3}}$ is the shear stress, Δv_τ is the relative velocity between the specimen and the anvil in the direction of the shear. The friction factor m can vary between the limits $0\le m\le 1$. The relative velocity, at $z=h$, is

$$\Delta v_\tau=v_r=\frac{1}{2}\xi_0 r-2r\left(a_1+a_2\frac{r^2}{R_{\max}^2}\right) \tag{10}$$

The frictional power becomes

$$W_\tau^*=m\frac{k_f}{\sqrt{3}}\int_0^{r_{\min}}\frac{1}{2}\xi_0 r-2r\left(a_1+a_2\frac{r^2}{R_{\max}^2}\right)dr \tag{11}$$

Calculation method. Substituting Eq. 7 and Eq. 9 into Eq. 2 gives the external supplied power.

$$J=2\pi k_f\int_0^h\int_0^{r_{contour}} r\bar{\xi}\,dr dz+m\frac{k_f}{\sqrt{3}}\int_0^{r_{\min}}\frac{1}{2}\xi_0 r-2r\left(a_1+a_2\frac{r^2}{R_{\max}^2}\right)dr \tag{12}$$

By the solution of Eq. 12 the externally supplied power is obtained as:

$$J = 2Fv_0 = 2pAv_0 \tag{13}$$

where F is the measured force during the compression, v_0 is the velocity of the anvil, p is the calculated pressure and $A = r_{\min}^2 \pi$ is the contact surface. The stationary value of variational function Eq. 2 is determined based on the Ritz method [6].

$$\begin{aligned} \delta J &= \frac{d}{da_1}\left\{ \dot{V}_{\cdot\cdot\cdot\cdot\tau} \quad \frac{\dot{H}}{da_1} + \frac{\dot{\cdot\cdot\cdot\cdot\tau}}{da_1} = 0 \right. \\ \delta J &= \frac{d}{da_2}\left\{ \dot{V}_{\cdot\cdot\cdot\cdot\tau} \quad \frac{\dot{H}}{da_2} + \frac{\dot{\cdot\cdot\cdot\cdot\tau}}{da_2} = 0 \right. \end{aligned} \tag{14}$$

The variational parameters a_1, a_2 can be determined as follows:

$$\begin{aligned} v_r\big|_{\substack{r=R_{\max} \\ z=0}} = v_{D\max} \quad &\rightarrow \quad \frac{1}{2}\xi_0 R_{\max} + R_{\max}\left(a_1 + a_2\right) = v_{D\max} \\ v_r\big|_{\substack{r=R_{\min} \\ z=h}} = v_{D\min} \quad &\rightarrow \quad \frac{1}{2}\xi_0 R_{\min} + 2R_{\min}\left(a_1 + a_2 \frac{R_{\min}^2}{R_{\max}^2}\right) = v_{D\min} \end{aligned} \tag{15}$$

where $v_{D\max}$ and $v_{D\min}$ are the velocity of the outer surface at point $R_{\max}$ and $R_{\min}$, respectively. From Eq. 14 and Eq. 15 the friction factors (m_1 and m_2), from Eq. 12 and Eq. 13 the flow stress can be determined. The solution gives two friction factor, one of them, with physical meaning ($0 \le m \le 1$), is used in the calculation of the flow stress. The calculated flow stress is compared to the results from the plane strain compression test.

Experiments

The experiments were performed with 6082M aluminium alloy. Cylindrical specimens were manufactured from the rod raw material, then annealed at 370°C through 2.5 hours. The cylindrical upsetting tests were made on Gleeble 3800 simulator. The velocity of the anvil was 1 (mm/s), the initial diameter (D_0) of the specimen was 10 (mm), the initial height (H_0) was 15 (mm) and the final height (H_f) was 8 (mm). The tests were performed with two layers of graphite foil on both contacting surfaces as lubricants. During the compression the change of D_{max} was measured by diametral extensometer. The experimental setup and the specimen before and after the deformation are shown in Fig 2.

Fig. 2 The experimental setup for cylindrical upsetting

Results and discussion

The key factor during the test the reliable measurement of the maximum diameter $D_{\max}$, in Fig. 3 the change of $D_{\max}$ is shown.

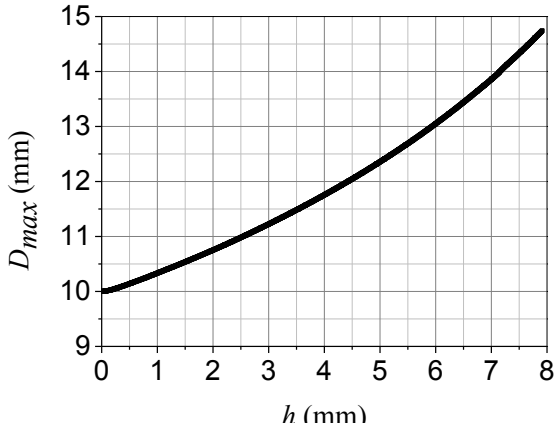

Fig. 3 Maximum diameter – height reduction (left) and force – height reduction (right) diagrams

The variational parameters and the friction factors are not constant during the compression, they are calculated in each state of the compression. The calculated values are shown in Fig 4.

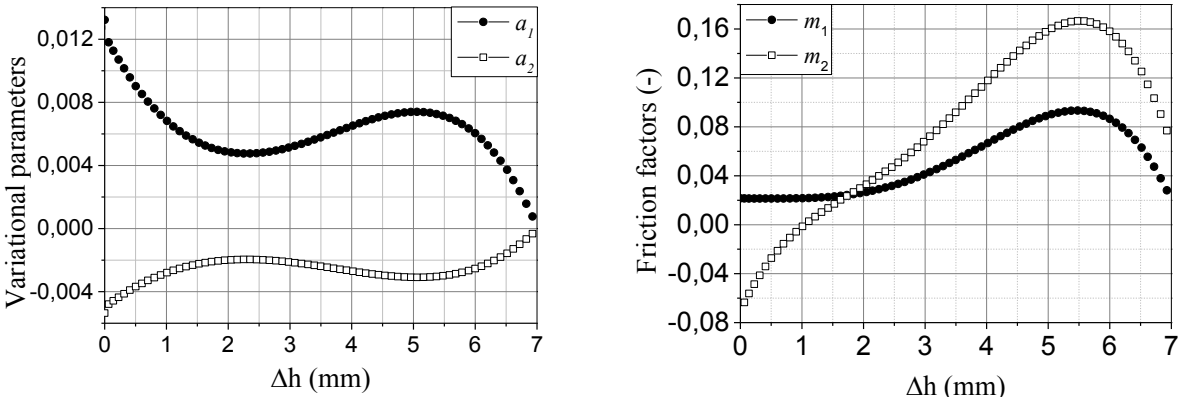

Fig. 4 Variational parameters – height reduction (left) and friction factor – height reduction (right) diagrams

The comparison between the plane strain compression test and the cylindrical upsetting test are shown in Fig. 5. The results of the plane strain compression test, which gives the best approximating flow stress curve, and the cylindrical upsetting tests are in good agreement in the equivalent plastic strain range of 0-0.7.

In a simple continuous compression test, barrelling occurs due to friction between the specimen and the die. Suitable lubricant may reduce the effect of friction, but never eliminate it. The correction of the effect of friction (barrelling), will improve the calculated flow stress results. In the case of unknown friction factor by measuring the maximum diameter and height, reliable results can be obtained by continuous cylindrical upsetting test in strain range of 0-0.7.

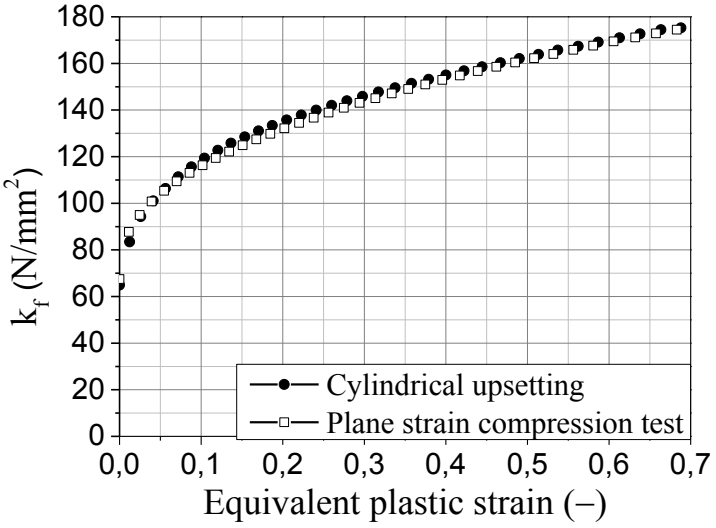

Fig. 5 Results obtained by plane strain compression test
and cylindrical upsetting with correction

References

[1] Rastegaev, M.V.: New Method of Homogeneous Upsetting of Specimens for Determining the Flow Stress and the Coefficients of Inner Friction – Zavodszkaja Laboratorija, N3 (1940) 354 (in Russian)

[2] Ettuney , O. Hardt, D.E.: A Method for in-Process Failure Prediction in Cold Upset Forging, Journal of Engineering for Industry, 105 (1983) 161-167

[3] Ebrahimi R., Najafizadeh A.: A New Method for Evalution for Friction in Bulk Metal Forming, Journal of Materials Processing Technology, 152 (2004) 136-143

[4] György Krállics, András Reé, Kristóf Bobor, Viktor Szombathelyi: Limitations in Measuring the Flow Stress, Materials Science Forum, Vol. 752 (2013) 85-94

[5] Kolmogorov, V.L., 1999. A method for calculating the stress-strain state in the general boundary-value problem of metal forming - part1. International Journal of Solids and Structures 36, 1253-1262.

[6] Keith, D.H., 2005. The Ritz Method of Approximation. Fundamentals of Structural Mechanics, 193-239.

Acknowledgements

This work is supported by the TÁMOP-4.2.2.A-11/1/KONV-2012-0027 project and by the Hungarian Scientific Research Fund, OTKA, Grant No. K-100500. The project is co-financed by the European Union and the European Social Fund.

On the topological characterization of fullerene-like materials using Zagreb indices-based topological descriptors

Tamás Réti[1*], István László[2] and Asma Hamzeh[3]

[1]Obuda University, Bánki Donát Faculty of Mechanical and Safety Engineering
Nepszinhaz u. 8., H-1080, Budapest, Hungary
[2]Budapest University of Technology and Economics, Institute of Physics
H-1520, Budapest, Hungary
[3]Tarbiat Modares University, Faculty of Mathematical Science
Department of Mathematics, P.OB. 14115-137 Tehran, Iran
*reti.tamas@bgk.uni-obuda.hu

Keywords: Fullerene, topological invariant, bidegreed graphs, stability prediction

Abstract. To classify quantitatively the topological structure of all carbon fullerene molecules (fullerene graphs) we suggest a novel two-step method based on the following concept: As a first step, the duals of the fullerene graphs are generated, and as a second step, by using two molecular descriptors called Zagreb indices, we construct appropriately defined topological indices for structural characterization of fullerene isomers. Performing comparative tests on the set of C40 fullerene isomers, it will be demonstrated that the method suggested can be efficiently applicable to the stability prediction of fullerene-like materials.

Introduction

A large number of topological graph invariants (called topological or molecular descriptors) are used for the quantitative characterization of molecular graphs. In the structural chemistry the two types of molecular descriptors called Zagreb indices belong to the family of the oldest and most studied topological invariants. They have been introduced more than thirty years ago by Gutman and Trinajstić [1]. Several results related to the successful application of Zagreb indices were communicated in the mathematical and chemical literature [2,3].

In this study, based on the use of Zagreb indices, a novel method for the structural characterization of fullerene graphs is presented. Performing a comparative test on the set of C40 fullerene isomers, it will be demonstrated that the method proposed can be efficiently applicable to the stability prediction of fullerene-like materials.

Theoretical considerations

The definition of Zagreb indices is based on the standard graph theoretical concept [1,2,3]: Let G be a simple connected graph with vertex number $|V|$ and edge number $|E|$, where V and E denote the finite set of vertices and edges of G, respectively. For a vertex u of G, the degree of u, denoted by d(u) is the number of edges incident to u. We denote by $\Delta = \Delta(G)$ and $\delta = \delta(G)$ the maximum and the minimum degrees of vertices of G. A graph is called r-regular if all its vertices have the same degree r. A graph is called irregular if it contains at least two vertices with different degrees.

Bidegreed graph is a connected non-regular graph whose vertices have exactly two degrees δ and Δ, where $\Delta > \delta \geq 1$.

Denoting by uv an edge of G, the first Zagreb index $M_1(G)$ and the second Zagreb index (M_2) of a graph G are defined as

$$M_1 = M_1(G) = \sum_{u \in V(G)} d^2(u) \qquad \text{and} \qquad M_2 = M_2(G) = \sum_{uv \in E(G)} d(u)d(v).$$

As can be seen, the first Zagreb index $M_1(G)$ is equal to the sum of squares of the degrees of the vertices, and the second Zagreb index $M_2(G)$ is equal to the sum of products of the degrees of pairs of adjacent vertices of the graph G.

Using the first and second Zagreb indices, four different topological parameters of graph G has been selected for the structural graph characterization:

$$\Phi = \Phi(G) = \frac{2M_2(G)}{M_1(G)} \tag{1}$$

$$\Omega = \Omega(G) = \sqrt{\frac{M_2(G)}{|E(G)|}} \tag{2}$$

$$IRM = IRM(G) = M_2(G) - \frac{4|E(G)|^3}{|V(G)|^2} \tag{3}$$

$$IRZ = IRZ(G) = \sum_{u \in V(G)} d^3(u) - 2M_2(G) \tag{4}$$

Zhou verified that for any connected graph G with a spectral radius ρ(G) the inequality $\Phi(G) \leq \rho(G)$ holds [4]. Moreover, the equality holds if graph G is regular or pseudo-regular [5]. The topological invariant Ω(G) can be considered as a possible approximation of the graph spectral radius. It has been shown that there exists a broad class of connected graphs for which the equality $\Omega(G) = \rho(G)$ is fulfilled.

The topological quantities IRM(G) and IRZ(G) belong to the family of the so-called graph irregularity indices [6,7,8]. From their definition it follows that both of them are non-negative numbers, and they are equal to zero if and only if graph G is a regular graph [9].

Characterization of dual graphs of fullerene isomers

A fullerene (fullerene graph) with k vertices, denoted by C_k exists for all even $k \geq 20$ except k=22, where the number of pentagon is 12, and the number of hexagons is k/2-10 [10]. In several cases, for the stability prediction of lower fullerene isomers C_k with $k \leq 70$ the so-called pentagon adjacency index N_P is used [10-14]. By definition, Np is equal to the total number of edges between adjacent pentagons. In other words, Np is identical to the number of fused pentagon pairs in an isomer.

Generally, it is supposed that fullerenes which minimize N_P are more likely to be stable than those that do not [10-14]. According to this hypothesis the buckminsterfullerene is the most stable C_{60} fullerene, because in the case of $20<k<70$, this is the only one for which N_P has a minimum value ($N_P=0$). However, in some particular cases the discriminating performance (i.e. the efficiency of prediction) of N_P index is limited.

A more efficient structural characterization of fullerenes can be performed if we use the dual graphs of the original fullerene graphs. This implies that the two-step method suggested for the structural characterization of fullerene graphs is based on an indirect approach.

In the first step, the duals of the traditional fullerene graphs are generated. The dual graphs of fullerenes are non-regular, bidegreed graphs, they contain 12 vertices of degree 5, and any remaining vertices are of degree 6. It is easy to show that for the dual graph C_k^{dual} of a traditional fullerene isomer C_k, the following equalities hold [15]:

$$\left|E(C_k^{dual})\right| = 3k/2 \tag{5}$$

$$\left|V(C_k^{dual})\right| = (k+4)/2 \tag{6}$$

$$M_1(C_k^{dual}) = 18k - 60 \tag{7}$$

$$M_2(C_k^{dual}) = 54k + Np - 360 \tag{8}$$

$$\sum_{u \in V(C_k^{dual})} d^3(u) = 108k - 660 \tag{9}$$

where Np is the pentagon adjacency index of a fullerene isomers.

Using the above formulas, for a traditional k-vertex fullerene isomer C_k, the following descriptors can be obtained as a particular case:

$$\Phi_d = \Phi(C_k^{dual}) = \frac{2M_2(C_k^{dual})}{M_1(C_k^{dual})} = \frac{54k + Np - 360}{9k - 30} < \rho(C_k^{dual}) < 6 \cdot \tag{10}$$

As can be seen, Φ_d is a linear function of Np index. Moreover,

$$\Omega_d = \Omega(C_k^{dual}) = \sqrt{\frac{M_2(C_k^{dual})}{\left|E(C_k^{dual})\right|}} = \sqrt{\frac{2M_2(C_k^{dual})}{3k}} = \sqrt{\frac{2(54k + Np - 360)}{3k}} \tag{11}$$

$$IRM_d = IRM(C_k^{dual}) = M_2(C_k^{dual}) - \frac{4\left|E(C_k^{dual})\right|^3}{\left|V(C_k^{dual})\right|^2} = M_2(C_k^{dual}) - \frac{54k^3}{(k+4)^2} \tag{12}$$

consequently,

$$IRM_d = 54k + Np - 360 - \frac{54k^3}{(k+4)^2} \cdot \tag{13}$$

For irregularity index IRZ_d, one obtains

$$IRZ_d = IRZ(C_k^{dual}) = \sum_{u \in V(C_k^{dual})} d^3(u) - 2M_2(C_k^{dual}) = 60 - 2Np \tag{14}$$

As can be seen, the pentagon adjacency index is included in each formula. That means that for a fixed vertex number k, the topological invariants given above can be directly calculated as a function of Np. However, from this observation it does not follows that for classical fullerenes the discriminating power of various topological descriptors is considered to be equivalent. It is interesting that the irregularity index IRZ_d is the only one which does not depend on the vertex number k.

Tests performed on the set of C40 isomers

We tested the discriminating performance of the five preselected topological descriptors (Np, Φ_d, Ω_d, IRM_d and IRZ_d) on the finite set of C_{40} fullerene isomers. Additionally, for comparative purposes, we computed the spectral radius R_d of the dual fullerene isomers, as well [16]. Simultaneously, using Density Functional Tight-Binding (DFTB) method [17] we calculated the total energy values TQ characterizing the relative stability of isomers.

Table 1 Computed topological descriptors and total energy values for forty C_{40} isomers.

Isomer	Topological parameter						Total energy TQ [eV]
	R_d	Φ_d	Ω_d	IRM_d	IRZ_d	Np	
C40:38	5.4890495	5.4848	5.4924	24.876	40	10	–342.031
C40:39	5.4897603	5.4848	5.4924	24.876	40	10	–341.631
C40:31	5.4913203	5.4879	5.4939	25.876	38	11	–341.438
C40:29	5.4917461	5.4879	5.4939	25.876	38	11	–341.345
C40:26	5.4918157	5.4879	5.4939	25.876	38	11	–341.094
C40:24	5.4922670	5.4879	5.4939	25.876	38	11	–341.022
C40:37	5.4910060	5.4879	5.4939	25.876	38	11	–340.636
C40:40	5.4927389	5.4909	5.4954	26.876	36	12	–340.580
C40:14	5.4946883	5.4909	5.4954	26.876	36	12	–340.476
C40:36	5.4910060	5.4879	5.4939	25.876	38	11	–340.431
C40:30	5.4939737	5.4909	5.4954	26.876	36	12	–340.304
C40:25	5.4945800	5.4909	5.4954	26.876	36	12	–340.277
C40:22	5.4947709	5.4909	5.4954	26.876	36	12	–340.230
C40:35	5.4917209	5.4879	5.4939	25.876	38	11	–340.196
C40:21	5.4956524	5.4909	5.4954	26.876	36	12	–340.151
C40:27	5.4937994	5.4909	5.4954	26.876	36	12	–340.126
C40:15	5.4944877	5.4909	5.4954	26.876	36	12	–339.943
C40:17	5.4960335	5.4939	5.4970	27.876	34	13	–339.884
C40:34	5.4936774	5.4909	5.4954	26.876	36	12	–339.827
C40:28	5.4944236	5.4909	5.4954	26.876	36	12	–339.777
C40:16	5.4964612	5.4909	5.4970	27.876	34	13	–339.645
C40:20	5.4957915	5.4939	5.4954	26.876	36	12	–339.627
C40:9	5.4977966	5.4939	5.4970	27.876	34	13	–339.614
C40:10	5.4977120	5.4939	5.4970	27.876	34	13	–339.558
C40:12	5.4970645	5.4939	5.4970	27.876	34	13	–339.370
C40:13	5.4976413	5.4939	5.4970	27.876	34	13	–339.347
C40:19	5.4962914	5.4939	5.4970	27.876	34	13	–339.292
C40:23	5.4972724	5.4939	5.4970	27.876	34	13	–338.690
C40:6	5.5011144	5.4970	5.4985	28.876	32	14	–338.624
C40:18	5.4989259	5.4970	5.4985	28.876	32	14	–338.341
C40:5	5.5020757	5.4970	5.4985	28.876	32	14	–338.332
C40:32	5.4994279	5.4970	5.4985	28.876	32	14	–338.270
C40:8	5.5046265	5.5000	5.5000	29.876	30	15	–338.113
C40:33	5.4999739	5.4970	5.4985	28.876	32	14	–337.922
C40:4	5.5039109	5.5000	5.5000	29.876	30	15	–337.348
C40:7	5.5029706	5.5000	5.5000	29.876	30	15	–337.330
C40:11	5.5019917	5.5000	5.5000	29.876	30	15	–336.642
C40:2	5.5086293	5.5030	5.5015	30.876	28	16	–336.489
C40:3	5.5160459	5.5091	5.5045	32.876	24	18	–335.193
C40:1	5.5260158	5.5151	5.5076	34.876	20	20	–333.806

The computed topological descriptors of dual fullerene isomers and the corresponding tight binding energy values (TQ) are given in Table 1. All of them were generated and sorted in terms of

the calculated total energy values. The number of topologically different C_{40} isomers is 40. Each isomer is labeled according to Fowler and Manolopoulos [10].

For C_{40} fullerene isomers, several topological descriptors have been already calculated [11-14]. Among the 40 isomers of C_{40}, C40:38 is predicted to be the isomer of lowest energy by many methods, this is followed by C40:39 and C40:31. The "least stable" isomer is C40:1 with Np=20.

As shown in Table 1, by using the topological descriptors (Np, Φ_d Ω_d and IRM_d) and the spectral radius of dual graphs (R_d), we obtained the same trends of relative stability, namely: C40:38 > C40:39> C40:31. This corresponds to the theoretical results based on ab initio calculations [11-14]. The discriminating performance of the descriptors Np, Φ_d, Ω_d and IRM_d are judged be equivalent for the set of C_{40} isomers.

It is important to note that the topological index IRZ_d gives a completely opposite stability ranking. Surprisingly, the least stable C40:1 isomer is characterized by the smallest irregularity index (20), while the most stable C40:38 and C40:39 isomers possess the largest irregularity index (40). This observation implies that the irregularity measures of different type are not necessarily compatible.

Summary

As a result of the comparative study performed on the set of C_{40} isomers, we can conclude, that the topological descriptors (Φ_d, Ω_d, IRM_d) correlate highly with the computed tight binding total energy values (TQ). All of them are efficiently used for the stability prediction of fullerene molecules.

Topological indices IRM_d and IRZ_d are indirect quantitative measures of the heterogeneity of original fullerene structures. In other words, both of them characterize the irregularity of the local arrangement of pentagonal and hexagonal faces in fullerene isomers. However, topological indices IRM_d and IRZ_d are not compatible. The irregularity measure IRZ_d gives a completely reverse order, consequently, it can not be used for the prediction of fullerene stability.

An additional advantage of the topological descriptors Φ_d, Ω_d and IRM_d is that they can be applicable to the structural characterization of non-classical fullerenes including square and heptagonal faces, as well.

References

[1] I. Gutman, N. Trinajstić, Graph theory and molecular orbitals. Total π-electron energy of alternant hydrocarbons, Chem. Phys. Lett. **17** (1972) 535-538.

[2] S. Nikolić, G. Kovačević, A. Miličević, N. Trinajstić, The Zagreb Indices 30 Years After, Croat. Chem. Acta, **76** (2003) 113-124.

[3] I. Gutman, Degree-Based Topological Indices, Croat. Chem. Acta, **86** (2013) 351-361.

[4] B. Zhou, Zagreb Indices, MATCH Commun. Math. Comput. Chem. **52** (2004) 113-118.

[5] A. Yu, M. Lu, F. Tian, On the Spectral Radius of Graphs, Linear Algebra Appl. **387** (2004) 41-49.

[6] L. Collatz, U. Sinogowitz, Spektren endlicher Graphen, Abh. Math. Sem. Univ. Hamburg **21** (1957) 63-77.

[7] V. Nikiforov, Eigenvalues and degree deviation in graphs, Linear Algebra Appl. **414** (2006) 347-360.

[8] T. Reti, D. Dimitrov, On Irregularity of Bidegreed Graphs, Acta Polytechnica Hungarica, **10** (2013) 117-134.

[9] A. Ilić, D. Stevanović, On Comparing Zagreb indices, MATCH Commun. Math. Comput. Chem. **62** (2009) 681-687.

[10] P. W. Fowler and D. E. Manolopoulos: *An Atlas of Fullerenes*, Calendron Press, Oxford, 1995.

[11] E.E.B. Campbell, P.W. Fowler, D. Mitchell and F. Zerbetto, Increasing cost of pentagon adjacency for larger fullerenes, Chem. Phys. Lett., **250** (1996) 544-548.

[12] E. Albertazzi, C. Domene, P.W. Fowler, T. Heine, G. Seifert, C. Van Alsenoy, F. Zerbetto, Pentagon adjacency as a determinant of fullerene stability, Phys. Chem. Chem. Phys. **1**, (1999) 2913-2918.

[13] P. W. Fowler, Resistance Distances in Fullerene Graphs, Croat. Chem. Acta, **75** (2002) 401-408.

[14] T. Réti, I. László, A. Graovac, Local combinatorial characterization of fullerenes, in: F. Cataldo, A. Graovac, O. Ori, (Eds.) *The Mathematics and Topology of Fullerenes,* Spinger Dordrecht, 2011, pp. 61-83.

[15] T. Došlić, T. Réti, D. Vukičević, On the Vertex Degree Indices of Connected Graphs, Chem. Phys. Lett. **512** (2011) 283–286.

[16] T. Réti, I. László, D. Dimitrov, Structural irregularity in fullerenes, *In Mathematical Chemistry Monographs, No. 16, Ante Graovac – Life and Works,* Eds. I. Gutman, B. Pokrić, D. Vukičević, (2014) in press.

[17] D. Porezag, Th. Frauenheim, Th. Köhler, G. Seifert, R. Kaschner, Construction of tight-binding-like potentials on the basis of density-functional theory: Application to carbon, Phys. Rev. **B51**, (1995) 12947-12957.

Simulation of Isothermal Austenitization in Banded Pearlite Steels by Cellular Automaton

Gábor Karacs[1, a], András Roósz[2, b]

[1]MTA-ME Materials Science Research Group, University of Miskolc,

H-3515 Miskolc-Egyetemváros, Hungary

[2]University of Miskolc, Institute of Physical Metallurgy, Metalforming and Nanotechnology,

H-3515 Miskolc-Egyetemváros, Hungary

[a]gkaracs@gmail.com, [b]femroosz@uni-miskolc.hu

Keywords: simulation, austenitization, cellular automaton, banded pearlite, finite difference method, nucleation, grain growth.

Abstract. The austenitization of steels can occur in a wide variety of initial microstructures. In this study we addressed the transformation of banded pearlite steels. Banded pearlite initial structures similar to the real ones were created. In these structures the entire transformation process was simulated whose part processes are nucleation and grain growth. The nucleation is described by a free energy based model, and the Fick II. diffusion equation by using Finite Difference Method describes the grain growth. These models have been coupled in cellular automata simulations.

Introduction

Ferrite and pearlite can appear in steels as alternating bands. Practically all hypoeutectoid steels show this pearlite/ferrite banding if the steel has been heavily deformed, followed by slow cooling from the austenite range. All wrought steels are heavily deformed by some method, usually a mixture of hot and cold rolling. If such steels are slow cooled and if they are sectioned parallel to the deformation direction, they will practically always appear banded. The banded appearance of the microstructure affects mainly the impact energy and the ductility of the steels, while other mechanical properties are not significantly altered. Microstructural banding is due to the segregation of substitutional alloying elements during dendritic solidification. Several investigations have shown manganese to be the alloying element most responsible for the development of microstructural banding in low alloy steels [1-3]. Moreover, austenitizing temperature, austenite grain size, and cooling rate influence the severity of microstructural banding.

Initial model microstructures I.

The first type of initial structures was made as follows: one-phase grain structures were created by using a grain coarsening simulation [4]. Smaller sub-grains could be developed by further grain-coarsening (Fig. 1) in these grains by modifying the simulation. The boundaries of the earlier grains indicate the former grain boundaries of austenite while the boundaries of the above smaller grains indicate the boundaries of pearlite colonies. The pearlite colonies can be obtained in such a way that the cementite lamellae having identical distance and thickness but different orientation are drawn into each sub-grain by the software by using its own algorithm. The lamellae can be made fragmented similar to the real structures. The banded pearlite initial structures were developed from these pearlite structures in such a way that horizontal ferrite bands were drawn on the previously obtained pearlite structure and using these bands as mask another one-phase grain structure was joint on the ferrite bands. We can see the obtained pearlite and banded pearlite structures in Fig. 1.

Initial model microstructures II.

Initial structures similar to the real ones can be developed by using microscopic images as well. An image taken of banded pearlite steel is shown in Fig. 2 The individual pearlite colonies cannot be

separated moreover the cementite lamellae cannot be seen so the following solution was chosen: the binary images are obtained by performing first the Otsu auto-detection [5] (Fig. 2).
In the images taken in such a way, the black colour indicates the pearlite and the white colour indicates the ferrite bands. The insignificant errors – tiny white points, black holes – can be cancelled by performing the opening and closing operations or just removing them from the images. Each black pixel indicates a pearlite colony in the binary image at the start. During the next step, the final pearlite colonies are developed by coarsening the many small pearlite colonies, and finally the cementite lamellae are drawn in the pearlite colonies (Fig. 2).

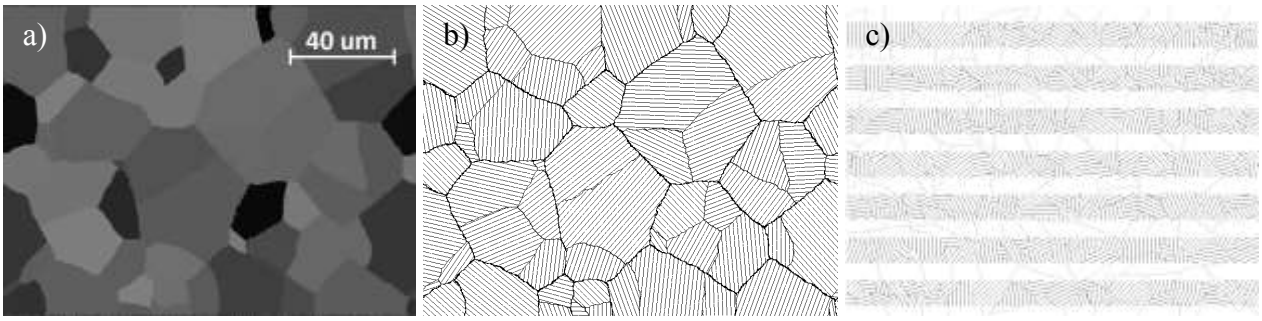

Fig. 1, Development of pearlite and banded pearlite structures (a, simulated grain structure with sub-grains, b, pearlite model structure, c, banded pearlite model structure

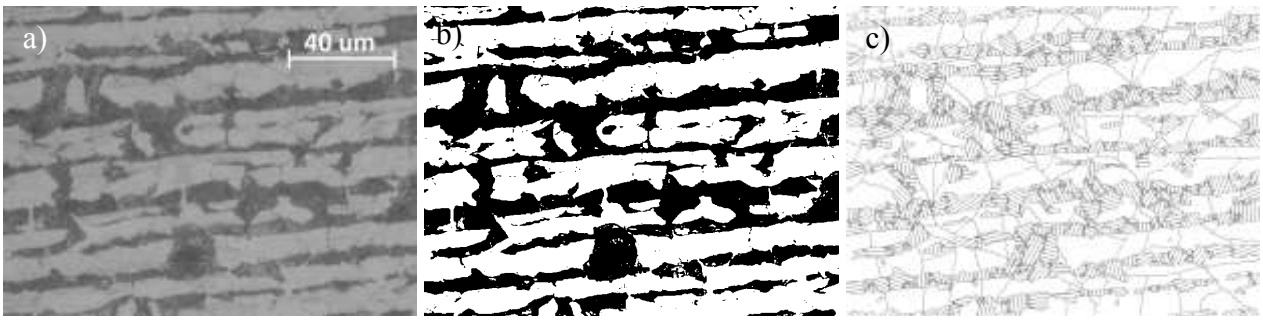

Fig. 2, Development of banded pearlite structure by using a microscopic image (a, grey image [6], b, detected binary image, c, structure to the real ones)

Model of nucleation.

The austenite nuclei can form at three types of ferrite/cementite interface: at the meeting of pearlite colonies (type 1), at the interface of ferrite and pearlite bands (type 2), and along the cementite lamellae inside the pearlite colonies (type 3). In practice the nuclei mainly form at the type 1 and 2 interfaces, as these places have higher free energy. Fig. 3 shows the three different places of nucleation.

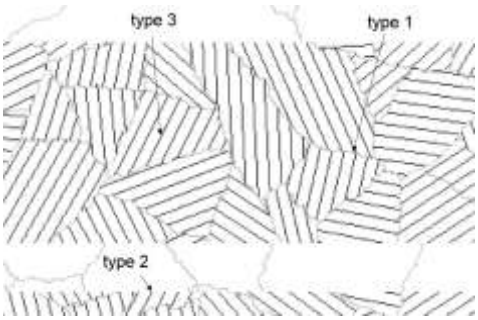

Fig. 3, Nucleation places in a banded pearlite model structure

The thermodynamic driving force of nucleation is the difference between the free energy of ferrite and cementite and the austenite:

$$G_V = G_\gamma - G_{\alpha+Fe_3C} \quad (1)$$

According to the model, each cell has a thermal free energy G_T (similar to the atoms) which follows the Maxwell-Boltzmann distribution. A free energy is optionally allocated to each cell at each time-step randomly [4]. By following the classical theory of nucleation, the nucleation rate is as follows:

$$I = K_1 N \frac{kT}{h} exp\left(-\frac{\Delta G_n + (\Delta G_D - \Delta G_{str})}{RT}\right) \quad (2)$$

$$\Delta G_n = \frac{16}{3}\pi \frac{y^3}{\Delta G_V^2} \quad (3)$$

$$\Delta G_V = L\frac{T_0 - T}{T_0} = L\frac{\Delta T}{T_0} \quad (4)$$

$$\Delta G_n = \frac{16}{3}\pi \frac{y^3 T_0^2}{L^2}\frac{1}{(T_0 - T)^2} = K_3 \frac{1}{(T_0 - T)^2} \quad (5)$$

$$I = K_2 exp\left(-\frac{1}{RT}\left(\frac{K_3}{(T_0 - T)^2} + \Delta G_D\right) + \frac{G_{str}}{RT}\right) = K_2 exp\left(-\frac{\sum \Delta G}{RT}\right) \quad (6)$$

where:
N – number of places of nucleation in a unit area, ΔG_n – activation free energy of nucleation, ΔG_{str} – free energy coming from the structure of interface, ΔG_D – activation free energy for transfer through the austenite/ferrite interface (approximated by the activation free energy of carbon diffusion in austenite, T – absolute temperature, T_0 – equilibrium temperature of transformation, k – Boltzmann-constant, R – general gas constant, h – Planck-constant, γ – surface energy at the austenite/ferrite interface, L – latent heat of transformation, K_1, K_2, K_3 – constants. Austenite can develop where $G_T > \sum \Delta G$.

The effect of parameters on the nucleation.

The simulations were performed in such a way that only one parameter was changed at one simulation; the other parameters were constants. The effects of the following parameters were investigated: ferrite/cementite interface free energies, temperature, carbon concentration, pearlite grain size number, pearlite interlamellar spacing.

The first linear section of curves flattening out later can be explained by the fact that at the beginning the nucleation places are free and therefore the nucleation rate is approximately constant (Fig. 4). However, fewer nuclei can develop as the number of free places decreases, and as a consequence the process slows and the nucleation places run out.

Fig. 5 shows the results of simulations performed using different interface free energies. Ever fewer nuclei of type 3 develop if the interface free energy decreases and at the end the number of type 3 nuclei will be lower than the number of type 1 nuclei. By increasing the interface free energy, the process displaces more and more towards the nucleation of type 3 taking place along the boundaries, because there are much more type 3 nucleation places than type 1 ones.

Fig. 6 shows that the nucleation rate decreases if the overheating decreases and it is equal to zero at the equilibrium temperature A_1. The curve can be approximated by an exponential function.

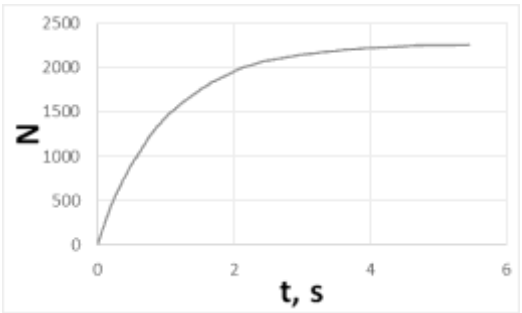

Fig. 4, Number of nuclei as a function of time

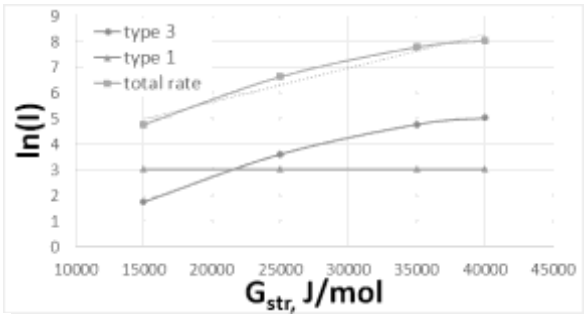

Fig. 5, Nucleation rate as a function of interface free energies

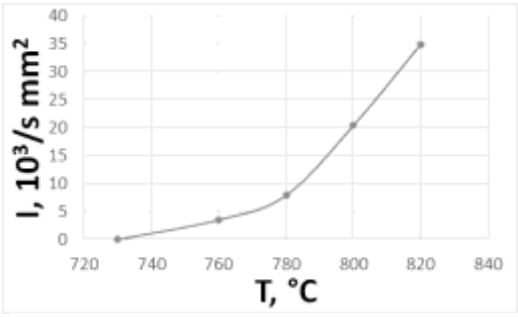

Fig. 6, Nucleation rate as a function of temperature

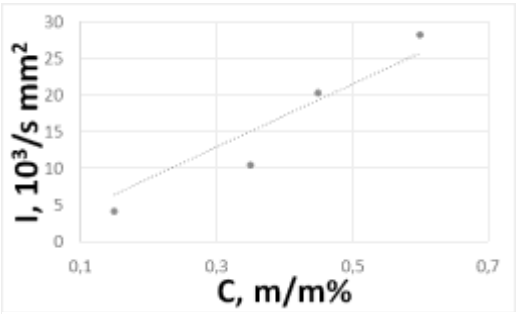

Fig. 7, Nucleation rate as a function of carbon concentration

The size of banded pearlite parts changes linearly by changing the carbon concentration, as a consequence the number of places of nucleation increases also near linearly so the nucleation rate changes near linearly as a function of concentration (Fig. 7).

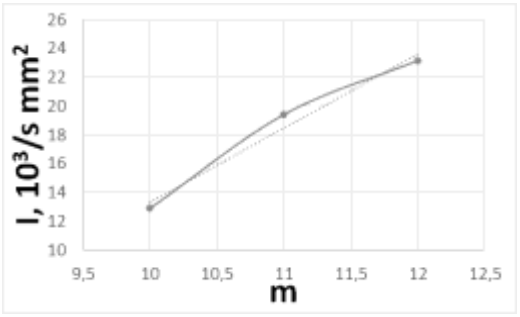

Fig. 8, Nucleation rate as a function of pearlite grain size

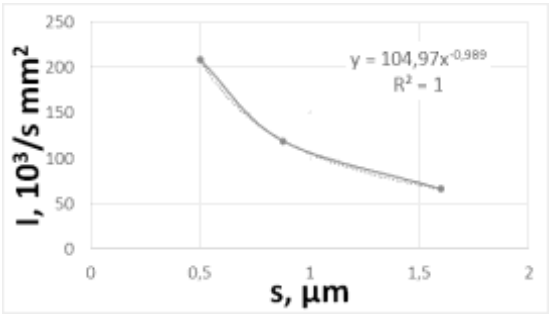

Fig. 9, Nucleation rate as a function of pearlite interlamellar spacing

By changing the size of pearlite colonies, as a consequence the quantity of pearlite-pearlite boundaries and the places of possible nucleation (type 1) changed as well. An approximately linear curve is kept for the nucleation rate as a function of grain size number (Fig. 8).
The number of possible nucleation places is inverse proportion of pearlite interlamellar spacing. If the interlamellar spacing is increased, due to the presence of less cementite lamellae the number of possible nucleation places is decreased and the nucleation rate will finally increase (Fig. 9).

Model of grain growth.

The growth of the γ phase is directed by the carbon diffusion through the γ and α phases (Fig. 10).
The dx change of the thickness of phases can be obtained by solving the following equation system (Eq. 7-11):

$$dx_y = \left(C_\gamma - C_\alpha\right) = D_\alpha \frac{\partial C_\alpha}{\partial x}|_{\alpha/\gamma}\, dt + D_\gamma \frac{\partial C_\gamma}{\partial x}|_{\alpha/\gamma} dt \tag{7}$$

$$dx_\alpha = -dx_y \tag{8}$$

$$dx^{Fe_3C}_{\alpha/Fe_3C} = \left(C_{Fe_3C} - C^{\alpha}_{\alpha/Fe3_C}\right) = D_\alpha \frac{\partial C_\alpha}{\partial x}|_{\alpha/Fe_3C}\, dt \tag{9}$$

$$dx^{Fe_3C}_{\gamma/Fe_3C} = \left(C_{Fe_3C} - C^{\gamma}_{\gamma/Fe3_C}\right) = D_\gamma \frac{\partial C_\gamma}{\partial x}|_{\gamma/Fe_3C}\, dt \tag{10}$$

$$\frac{\partial C_\alpha}{\partial t} = D_\alpha \frac{\partial^2 C_\alpha}{\partial x^2} \; and \; \frac{\partial C_\gamma}{\partial t} = D_\gamma \frac{\partial^2 C_\gamma}{\partial x^2} \tag{11}$$

The used concentrations are demonstrated in Fig. 10. The carbon concentrations of the different phase boundaries were calculated by using the ESTPHAD method [7]. The equation system was solved by the explicit Finite Difference Method. 600x800 cells were taken into consideration in the

two-dimensional model. By supposing the Neumann-neighbourhood, the concentration of the i,j^{th} cell in the h^{th} time step is as follows:

$$C_{i,j}^{h} = \frac{D\Delta t}{\Delta x^2}\left(C_{i-1,j}^{h-1} + C_{i+1,j}^{h-1} + C_{i,j-1}^{h-1} + C_{i,j+1}^{h-1} - 4C_{i,j}^{h-1}\right) + C_{i,j}^{h-1} \quad (12)$$

where:
h – number of Cell Automation Step (CAS), i – cell rows, j – cell columns, D – diffusion coefficient, Δt – one time step, Δx – size of one cell.

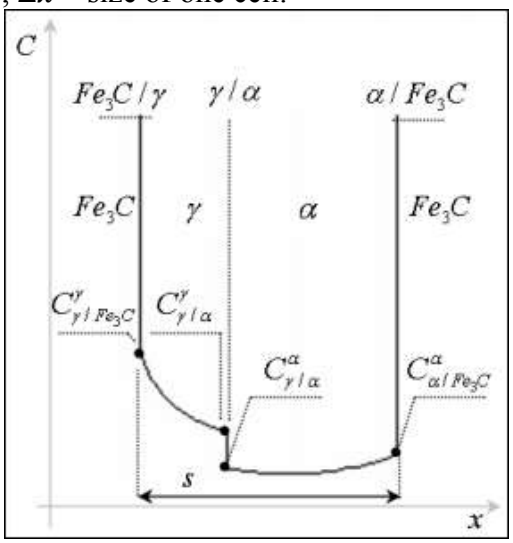

Fig. 10, Carbon concentrations at the α/γ, α/Fe_3C and γ/Fe_3C boundaries

Simulation of the whole process.

The whole process can be simulated by the common use of the models of nucleation and grain growth. The transformation of a banded pearlite structure can be seen in Fig. 11. The transformed ratio F of the initial structure is given by the Avrami-law as a function of time:

$$F = 1 - exp(-kt^n)$$

where:
k – constant as a function of time, n – Avrami-exponent.
It can be seen that the austenite grains grow faster in the direction of pearlite colonies, and slower to the ferrite because its lower carbon concentration. Hence the transformed structure will also be directional. From the obtained data the specific TTT diagram is represented (Fig. 12).

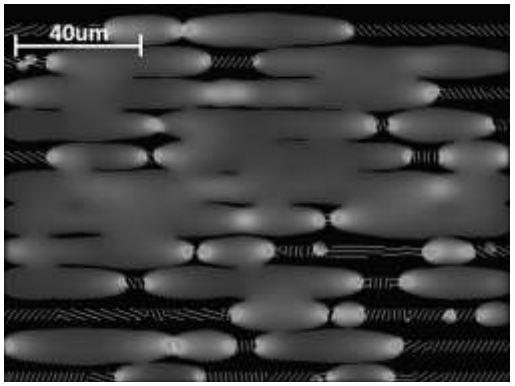

Fig. 11, Partially transformed banded pearlite structure

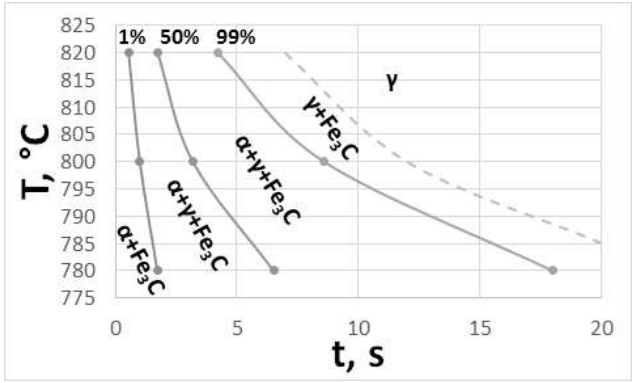

Fig. 12, Time-temperature-transformation (TTT) diagram of banded pearlite structure

Summary

This simulation is suitable for describing the isothermal austenitization in case of unalloyed hypoeutectoid, eutectoid and hipoeutectoid steels. It was shown that how the nucleation and grain growth occur in case of banded pearlite structures. In comparison with other models [8-11], the significant difference is that in this case a real lamellar structure is used instead of a simplified initial one. The simulation of the whole process is not restricted only to the transformation of the ferrite, the nucleation takes place both in the direction of the banded pearlite and the ferrite in the structures.

Acknowledgement

The research work presented in this paper based on the results achieved within the TÁMOP-4.2.1.B-10/2/KONV-2010-0001 project and carried out as part of the TÁMOP-4.2.2.A-11/1/KONV-2012-0019 project in the framework of the New Széchenyi Plan. The realization of this project is supported by the European Union, and co-financed by the European Social Fund.

References

[1] R. A. Grange, Effect of microstructural banding in steel, Metall. Trans. 2 (1971) 417–426.
[2] R. Grossterlinden, R. Kawalla, U. Lotter, H. Pircher, Formation of pearlitic banded structures in ferritic-pearlitic steels, Steel Res. 63 (1992) 331–336.
[3] V. Faccenda, M. Falco, C. Modena, Metall. Ital. 65 (1973) 133–140.
[4] J. Geiger, A. Roósz, P. Barkóczy, Simulation of grain coarsening in two dimensions by cellular-automaton, Acta Mater. 49 (2001) 623-629.
[5] Nobuyuki Otsu, A threshold selection method from gray-level histograms, IEEE Trans. Sys., Man., Cyber. 9 1 (1979) 62–66.
[6] Information on http://www.bladesmithsforum.com
[7] A. Roósz, J. Farkas, Gy. Kaptay, Thermodynamics-based semi-empirical description of the liquidus surface and partition coefficients in ternary Al-Mg-Si alloy, Materials Science Forum 414-415 (2003) 323-328.
[8] A. Jacot, M. Rappaz, A combined model for the description of austenitization, homogenization and grain growth in hypoeutectoid Fe–C steels during heating, Acta Mater. 47 (1999) 1645-1651.
[9] B. J. Yang, L. Chuzhoy, M. L. Johnson, Modeling of reaustenitization of hypoeutectoid steels with cellular automaton method, Computational Materials Science 41 (2007) 186-194.
[10] Shtansky, D. V., Nakai, K., Ohmori, Y., Pearlite to austenite transformation in an Fe–2.6Cr–1C alloy, Acta Mater. 47 (1999) 2619–2632.
[11] Yang, B. J., Hattiagandi, A., Li, W. Z., Zhou, G. F., McGreevy, T. E., Simulation of steel microstructure evolution during induction heating, Mater. Sci. Eng. A 527 (2010) 2978–2984.